A CASE STUDY FROM THE ZAGROS AREA IN SOUTHWEST IRAN EXAMINES THE GEOCHEMISTRY, FACIES FEATURES, AND PALAEOENVIRONMENTAL CIRCUMSTANCES OF THE STORM-DOMINATED PHOSPHATE-BEARING DEPOSITS OF THE EASTERN TETHYAN OCEAN

Armin Salsani[1], Abdolhossein Amini[2],*, Shahram shariati[3], Seyed Ali Aghanabati[4], and Mohsen Aleali[1]

[1]Department of Geology, Science and Research Branch, Islamic Azad University, Tehran, Iran
[2]School of Geology, College of Science, University of Tehran, Tehran, Iran
[3]Department of Geology, Sari branch, Islamic Azad University, Sari, Iran
[4]Earth Sciences Research Institute, Geological Survey of Iran, Tehran, Iran

Abstract

The South Tethyan Phosphogenic Province, a vast carbonate-dominated stratum that stretches across the Middle East, has phosphate resources in south-western Iran. The Tethyan phosphorites of Iran are classified as low-grade ore deposits globally and date to the Eocene-Oligocene (Pabdeh Formation). The Pabdeh Formation was formed on a carbonate ramp setting as a distally steepened ramp, according to the depositional conditions of the facies. In such a setting, turbidity currents carried phosphate particles from the deeper middle and outer ramp of the ocean to the back-shoal setting where they were suspended and deposited as shell-lag and phosphate lamination. Microfacies investigations show that turbidity currents helped all the phosphatic ooids and phosphatized foraminifera, fish scales, bones, and phosphatic intraclasts relocate from shallow to deeper sections of the Tethyan Ocean. REE+Y and P2O5 exhibit a positive correlation in all analyzed sections, which attests to their high geochemical group coherence, according to analysis and interpretation of the data. Negative Ce anomalies define the shale normalized REE patterns of Mondun phosphorites. In contrast, Nill sections with Ce enrichment suggest circumstances of somewhat deeper water sedimentation. This anomaly indicates that the depositional environment was oxic and intensively reworked, bioturbated with greater energy levels during phosphate deposition. These geochemical results are consistent with microfacies analyses, which show that the Mondun section is in a shallow and high energy state with negative cerium anomalies, whereas the Nill and Siah sections are in a deep ramp setting with positive cerium anomalies in REE patterns.

Key words: shell-lag; turbidity currents; rare-earth elements; yttrium; Tethyan phosphorites; Pabdeh Formation

1. Introduction

Around 1800 km long and 150 km broad, the Zagros fold and thrust belt stretches from south Turkey through Iraq to southwest Iran. The belt, which is connected to a foreland basin, is the region's oldest and richest hydrocarbon zone [1]. Potential oil deposits are believed to exist in the underlying Gurpi Formation and the late Palaeocene to early Oligocene Pabdeh Formation. The top of the Gurpi Formation is the Pabdeh Formation, which is overlain by a very weathered, glauconitic-rich layer that is thin (1-3 m), purple, sandy to silty, and suggests a major unconformity [2]. For this unconformity, palaeontological evidence points to a missing era of roughly 10 my [3].

The research area's Pabdeh Formation, which is abundant in planktonic microfauna, is made up of thin- to thick-bedded limestones that alternate with dark- to light-gray shales and green- to-gray marls. This formation is defined as a fine-grained, matrix-rich, carbonate-dominated succession with some hydrocarbon source potential in the majority of the Zagros, particularly in the Dezful embayment [4-6]. The Pabdeh Formation hasn't received much attention for its phosphate-bearing horizons, despite several studies on its prospective oil reserves.

In the best outcrops in the Zagros area, this research examines the facies features, precise potential, and depositional circumstances of the phosphate-bearing strata of the Pabdeh formation.

This study emphasizes the fundamental similarities and differences between the phosphate-bearing horizons by concentrating on the Pabdeh Formation's phosphate-bearing horizons and presenting the first completely integrated geochemical assessment of the Pabdeh Formation. The abundances of main, trace, and rare-earth elements as well as their distribution patterns and inter-element connections are discussed in this study.

2. Geological setting and stratigraphy

The Zagros band, an Alpine-Himalayan orogenic belt, includes the NW-SE trending Iranian Mountains in west and southwest Iran [7]. In the Zagros belt, which dates from the very late Precambrian to the Late Miocene, discontinuous deposition took place along the NE border of the Arabian plate [2,8].

The Persian Gulf and continental Mesopotamia basins, which are the present-day manifestations of the Zagros (peripheral) proforeland system, and the underlying preproforeland, primarily platformal and continental shelf deposits, are both responsible for the structural deformation that led to the formation of this fold and thrust belt. The closure is connected to the Late Cretaceous formation of the Central Iran block beneath the Arabian Plate subduction [2,8,13,14]. The collisional mountain-building process, which got started in the Middle Maastrichtian (about 68 Ma), has since continued intermittently [2]. The Zagros foreland basin, which has sedimentary evidence from the Late Cretaceous to the present, was created as a result of this collision, which also caused the closure of the Neo-Tethys basin [15].

In the Zagros foreland basin throughout the Early Eocene to Oligocene, calcareous shale, marl, and lime mudstone with subordinate argillaceous limestone were deposited to form the deep-marine Pabdeh Formation. The majority of studies [16–19] link the formation's depositional environment to a ramp setting. Several locations show signs of a deep marine environment [20] and pelagic conditions with shared gravity fluxes [21]. (Figure 1).

Both Mohseni and Al-Aasm [17] and Mohseni et al. [18] discovered proof of storm deposition and sea currents during the Pabdeh Formation's late depositional phases. Moreover, a few carbonate tempestites were noted in the formation's stratigraphic record [17,22-30].

Tethyan phosphorites are only found in the Eocene-Oligocene Pabdeh Formation in Iran. The Pabdeh Formation's phosphatic strata are regarded as low-grade mineral resources worldwide. Pabdeh's phosphate deposits typically range from 8 to 12% P2O5, whereas Tethyan phosphorite deposits often range from 25 to 30%.

Journal of New Zealand Studies NS35 (2023), https://doi.org/ 10.5281/zenodo.7805493

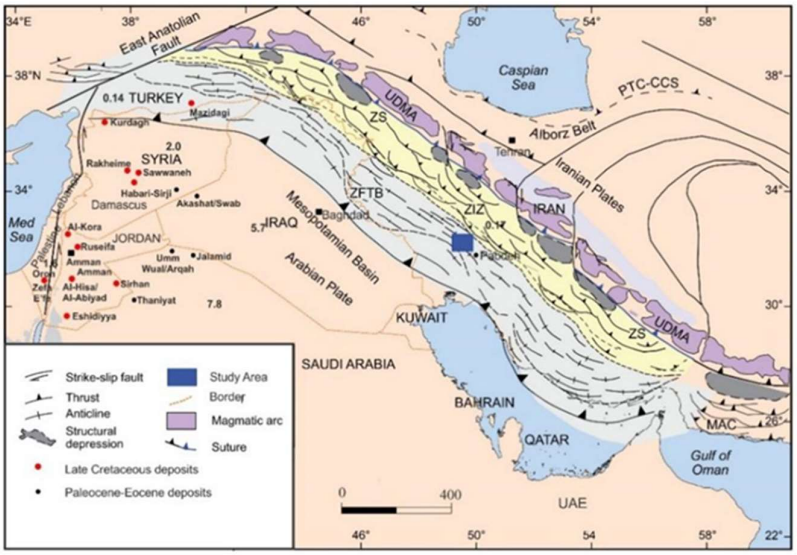

Figure 1. This shows the locations, ages, and total resources of the principal phosphorite deposits in the eastern Mediterranean area and the neighboring nations (bold numbers in billion tonnes) [31]. the Zagros Orogenic Belt's divisions. (Altered from [15]). Paleo-Tethyan continent-continent collisional suture (PTC-CCS), Uremiah-Dokhtar magmatic assembly (UDMA), Zagros fold-and-thrust belt (ZFTB), Zagros imbricate zone (ZIZ), Zagros suture (ZS), and Makran accretionary prism (MAC) are some of the terms used to describe this region.

More than half of the world's phosphorite deposits, or roughly 80 billion tonnes of high-grade commercial phosphorites, are found in the eastern Mediterranean area and North Africa [32–34]. These deposits are a component of the Late Cretaceous to Eocene Tethyan Phosphorite Regime, which also includes areas of the Caribbean, Columbia, and Venezuela in northern South America, as well as North and Northwest Africa [31,35-39]. The largest phosphorite deposits in the eastern Mediterranean region and throughout the Tethys realm were formed as a result of these tectonic events [31].

The Akashat Formation in Iraq, the Jalamid, Mira, and Umm Wu'al and Dammam Formations in Saudi Arabia, Sawwaneh, Rmah, and Bardeh Formations in Syria, Mishash (Palestine), Thelja (Tunisia), Vilga, Abu Tarbur, Al-Hisa (Jordan), and Usfan (Saudi Arabia) are all related to the Mediterranean phosphatic belt formations (Figure 1).

Much of Iraq's western regions are exposed to the Akashat Formation. This Formation is made up of phosphatic conglomerate or breccia mixed in with grey phosphorites and limestones [41]. The depositional environment is subtidal, warm, and represents the inner to outer shelf.

The Dammam dome in Saudi Arabia is the location of the Dammam Formation's type locality [40]. This Formation, which Bramkamp [42] uncovered, is composed of a series of carbonates from shallow sea shelf sediments interbedded with marls.

The higher portion of the Mishash Formation contains the majority of the economic phosphorites from Palestine. The topmost layer of the shallow marine epicontinental sediments in the Negev area of Palestine phosphorites is made up of the late Campanian-aged Mishash Formation [43,44].

One of the world's top producers of rock phosphate is Tunisia. Significant phosphorite deposits dating from the Paleocene to early Eocene are reported in Tunisia's Gafsa basin [45]. The sedimentary rocks are from the Metlaoui group [46], more specifically, they are from the Thelja

Journal of New Zealand Studies NS35 (2023), https://doi.org/ 10.5281/zenodo.7805493

Formation [47], which is followed by the Chouabine Formation and the El Haria Formation [46]. (Figure 2).

Massive phosphorite layers alternate with marly limestone, marls, and layers rich in silica in the Ypresian Chouabine Formation [48–53]. In the Gafsa-Metlaoui Basin, sedimentation took place in a somewhat constrained environment that alternated between lagoonal and littoral conditions, leading to rhythmic or episodic sedimentation [52,53]. Evaporitic cycles with shallowing-upward trends make up the Thelja Formation. With no slope deposits along a gently sloping platform, the Thelja Formation series' nine major facies exhibit a progressive shift from offshore marine facies to Sebkha facies [54]. (Figure 2).

The South Tethyan Phosphogenic Province (STPP), a vast carbonate-dominated Upper Cretaceous to Eocene phosphorite strata that stretches from Colombia to Venezuela, north and northwest Africa, and the Middle East, has phosphorus deposits in south-western Iran [37].

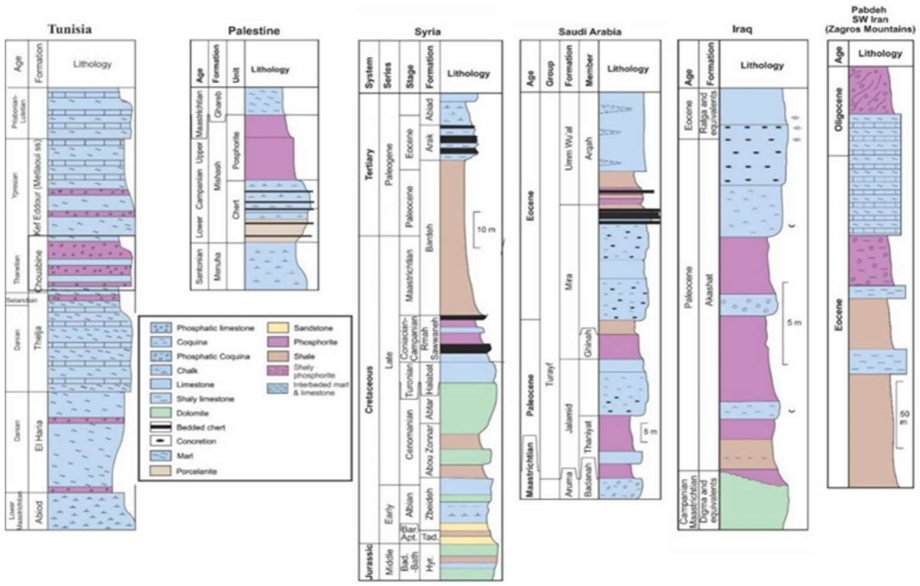

Figure. 2. Iraq, Iran, Syria, Saudi Arabia, Tunisia, and Palestine's Paleocene-Oligocene phosphate-bearing horizons: Lithostratigraphy (Modified from [31]).

Only the southeast of Syria contains high-grade phosphorites. The Rmah Formation is made up of fossiliferous interbedded marl, limestone, dolomite, and some chert nodules. Bedded chert, limestone, and thin phosphorite units alternately cover the top of the formation. The main phosphorite deposits in Syria may be found in the Sawwaneh Formation. Marly limestone and phosphorites are interspersed throughout the strata. A glauconitic-phosphatic marl is deposited on top of the marl and marly limestone that make up the formation's upper portion.

The Turayf Group's Hazm El-Jalamid, Mira, and Umm Wu'al Formations (Paleocene and middle Eocene) have phosphate deposits in northern Saudi Arabia (Figure 2). The phosphorite beds can have up to seven distinct beds and have total thicknesses between 3 and 5 meters [55]. The Hazm Al-Jalamid phosphorites have undergone sedimentary facies investigation, which indicates that they are transgressive lag deposits that formed in an oxic, bioturbated, and wave-dominated shelf environment that resulted from the Campanian incursions of Tethys [56].

The aforementioned data suggests that the phosphate horizons of the Pabdeh Formation were

formed in a deep marine environment, in contrast to the eastern Mediterranean region and north and northwest Africa, where phosphate deposits formed in shallow marine depositional environments and evaporitic cycles. According to a palaeogeographic map, the state is consistent with the Tethyan Phosphorite Regime, which stretches from north and northwest Africa across the eastern Mediterranean (Figure 3).

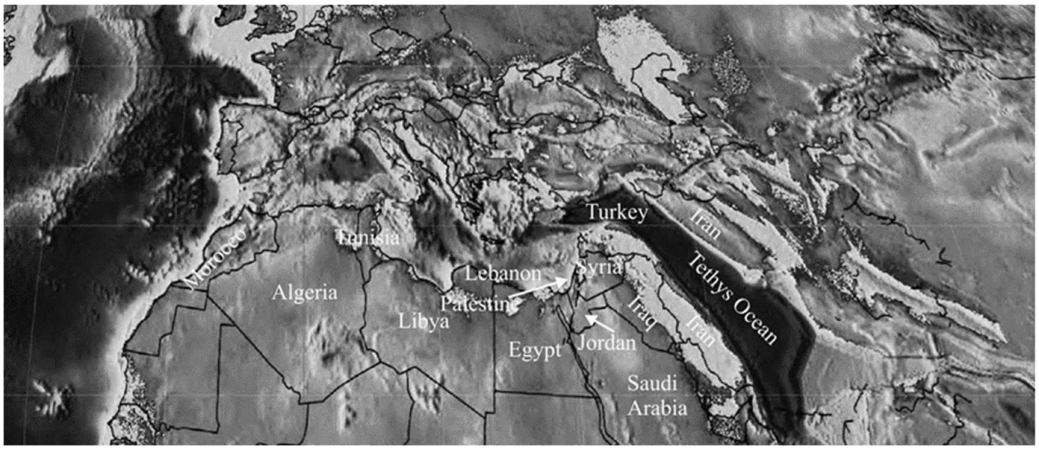

Figure 3. Early Middle Eocene (44.5 Ma—Middle Lutetian) palaeogeographic map showing the Tethyan Ocean's extent. The Tethyan Phosphorite Regime stretches from north and northwest Africa into the eastern Mediterranean. Country borders are shown by black lines [57].

The finest outcrops of the Pabdeh Formation are found in the study area, which is situated in the Zagros fold. In this investigation, the formation's three sections—Nil, Siah, and Moundun—with a combined thickness of 1122 m were examined (Figure 4). With a total thickness of 512 m, the formation in the Nil anticline (115 km north of the city of Gachsaran) is mostly composed of interbedded thin to medium limestone, marl, and dark grey shale. The formation in the Siah Anticline (60 km north of Gachsaran) is made up of 255 m of thin to medium-bedded limestone interbedded with shale and marl.

The 355 m thick Pabdeh Formation in the Mondun Section (85 km north of Gachsaran) is composed of interbedded shale, marl, and thin bedded limestone from the middle to the top of the formation. In the examined parts, the formation, which is Early Eocene to Oligocene in age, is located above the Late Cretaceous Gurpi Formation and is overlain by the Oligo-Miocene Asmari Formation.

Journal of New Zealand Studies NS35 (2023), https://doi.org/ 10.5281/zenodo.7805493

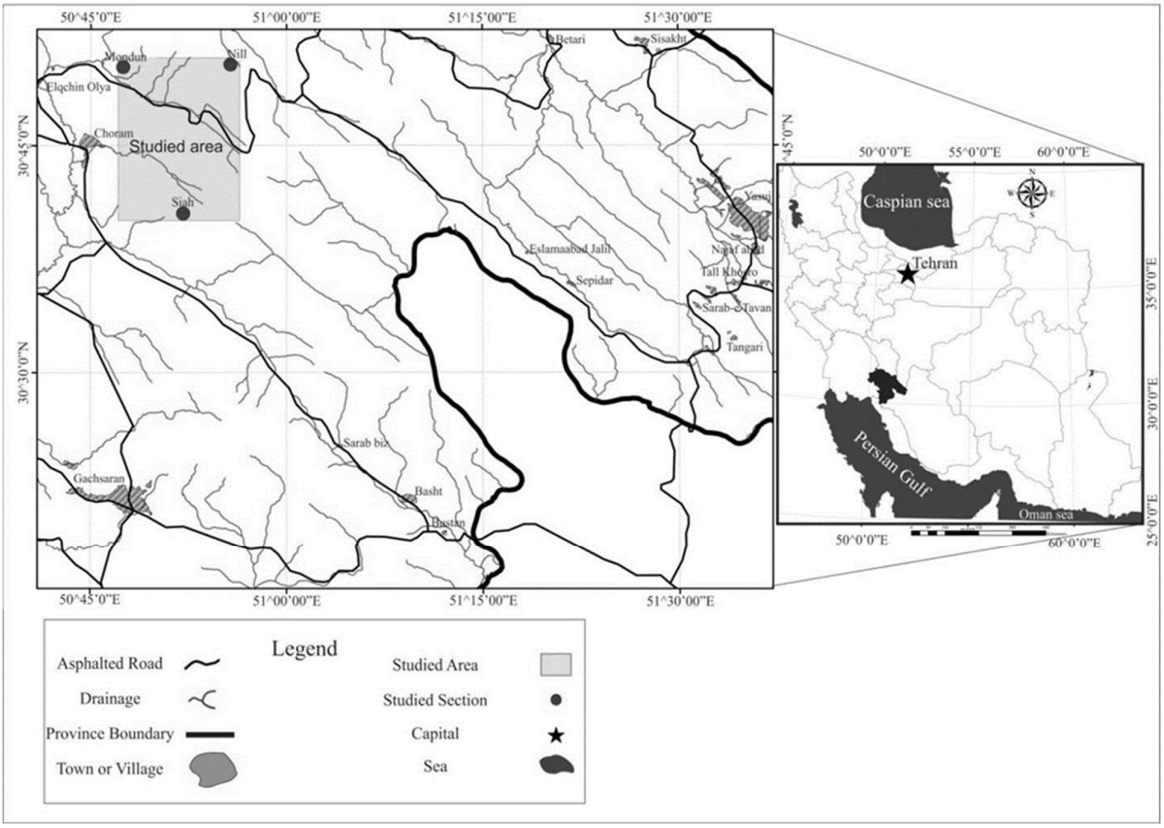

Figure 4. Regional and location maps showing the study area in the Zagros region (SW Iran).

2.1. The Nill section

The Gurpi, Pabdeh, and Asmari formations are exposed in the well-developed anticline known as the Nill Mountain. The Gurpi Formation, which is composed of thin to medium-thick strata of grey marl interspersed with thin layers of argillaceous limestone, is found near the bottom of the section. It is 6 m thick. Globotruncana sp. and other pelagic facies predominate in this formation, according to the results of petrographic research (see Supplementary) The dark grey shale unit has not been exposed, and the Gurpi Formation is unevenly overlain by strata of the Pabdeh Formation's thin-bedded limestone and dark grey shale. The Asmari Formation conformably overlies the Pabdeh Formation in this region, according to field evidence. In the Asmari Formation's base, marl and medium- to thick-bedded limestone alternate, eventually becoming thick-bedded limestone (Figure 5).

Journal of New Zealand Studies NS35 (2023), https://doi.org/ 10.5281/zenodo.7805493

Figure 5. The Nill anticline's top limit of the Pabdeh Formation may be seen in a field view, where medium to thick bedded limestone and marl alternate with thick bedded limestone.

Black shales and bioturbated argillaceous limestone alternate in the Pabdeh Formation in the Nill area. Limestone, green marls, and dark gray marls alternate in rhythm. The summit of the Formation is made up of alternating, thicker marls and limestone layers that are rich in benthic foraminifera. Within the Formation, three phosphatic units formed and were divided by alternating beds of thin-bedded limestones and dark-gray shale. The phosphatic beds have an average thickness of 12 m. At an average thickness of 6 m, phosphatized limestone dominates the first phosphatic horizon. The second phosphatic horizon has a total thickness of 2 meters and is composed of thin bedded limestone intercalated with phosphatized shale and marl (Figure 6). Four meters thick is the third phosphatic horizon. The phosphatic strata have an average grade of 2.94% P2O5. According to biostratigraphic analyses of planktonic foraminifera and the presence of Orbulinoides beckmani (Supplementary), the second and third units are, respectively, Lutetian and Bartonian in age.

Journal of New Zealand Studies NS35 (2023), https://doi.org/ 10.5281/zenodo.7805493

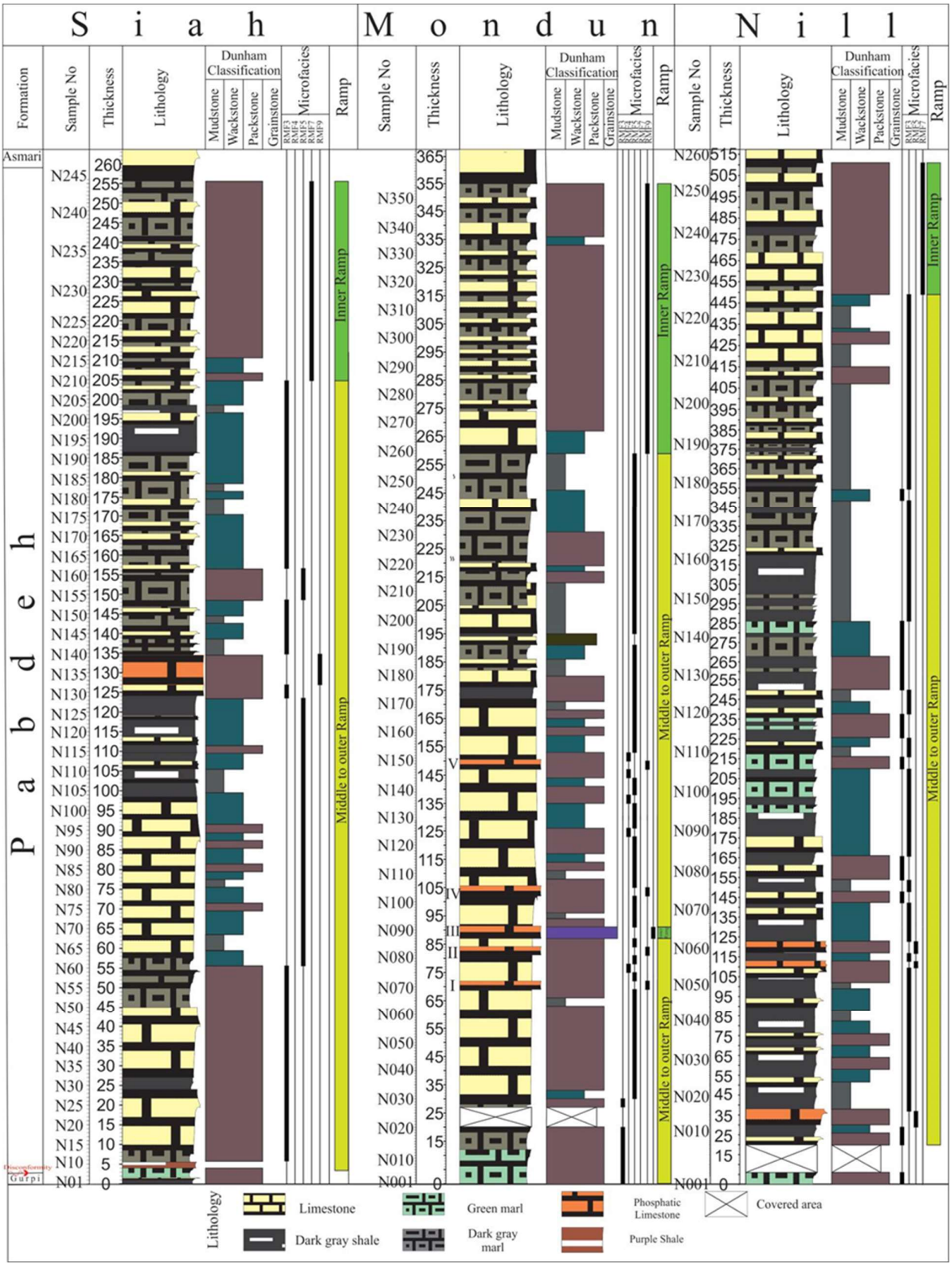

Figure 6. Stratigraphic and microfacies column of the Pabdeh Formation in the Nill, Mondun and Siah anticlines.

The Mondun section (2.2)

85 km to the north of Gachsaran is where the NW-SE trending Mondun Anticline may be found.

The Gurpi limestones are found underneath the Pabdeh Formation (355 m), which is present in this anticline with a clear unconformity. On the basis of the sedimentological properties and the presence of fossils, the formation is classified into four stratigraphic units (Figure 6). The Pabdeh Formation's bottom portion is greenish grey marl with thin interlayers of argillaceous cream limestone since the purple shale unit at its base has not been revealed in this outcrop (25 m thick). Hantkenina nuttalli, Pseudohastigerina wilcoxensis, Dentoglobigerina yequaensis, and Globigerinatheka index are found in the foraminiferal fauna (Supplimentary). Limestone with thin to medium bedded limestone denotes the second stratigraphic unit (120 m).
This horizon is of Early Eocene (Ypresian) age since it contains planktonic foraminifera such Acarinina wilcoxensis, Acarinina collactea, Acarinina bullbrooki, and Pesudohastigerina wilcoxensis (Supplementary). Dark grey shale, grey marls, and thin bedded limestones alternately layer to form the third stratigraphic unit, which is 50 m thick. Greenish grey shale predominates in the fourth half of the formation (135 m), with thin to medium bedded beige to yellow pelagic limestone intercalating. This area is the formation's highest point. According to microfacies research, the grainstone is bioclastic, phosphatic, foraminiferal, and oolitic (See section 4.3.1). Bioclastic packstone with laminated and phosphatized bedding is seen in all four horizons.

Five stratigraphic levels (layers I–V in Figure 6, from bottom to top) include the phosphatic horizons, which are separated by thin bedded planktonic limestones that are foraminiferal-rich. Limestone that has been phosphatized makes up all phosphatic horizons. They often have high P concentrations (III and IV 23% P2O5) and high carbonate contents (mostly calcite). The first and second horizons (I and II) were made up of alternating laminae that were rich in phosphate and rich in carbonate. These horizons have P2O5 grades of 5.51% and 5.08%, respectively. The third phosphorite horizon is made up of a facies of grainstone that is one meter thick and contains tiny phosphatized pellets, ooids, intraclasts, planktonic foraminiferal tests, fish scales, and bones with an average P2O5 content of 25.12%. The primary allochems in this well-sorted facies are mostly superficial ooids and pellets (See section 4.3.1). Foraminiferal tests, fish scales, and bones are minor allochems (Figure 7). The presence of ooid and pelletal phosphatized grains is the third phosphatic layer's (III) most distinguishing characteristic. The medium-sized (>200 m) phosphate grains, varying quantities of phosphatized intraclasts, fish scales, and bones are the characteristic components of the phosphate part of this horizon. The fourth and fifth (V) phosphorite horizons share Shell-lag bedsand as a common characteristic, and their average grades are 22.32% and 4.12%, respectively. The phosphatic beds often have a total thickness of 5 m. The Mondun phosphorite units in the research region exhibit greater lithological and facial diversity than the others (See section 4.3.1). They have unique high-grade mineralization at certain layers and are light brown, lithified, phosphatized pellet and locally phosphatized granular beds that are rich in oolites. All horizons' phosphatized strata have an average P2O5 grade of 12.43 percent.

Figure 7. Field view from the Mondun section showing fish-scale in the third phosphorite unit.

The Siah area

The Pabdeh Formation is 255 m thick and is located on the Siah anticline's northern side, 60 km north of Gachsaran. On the basis of the sedimentological properties and the presence of fossils, the formation is classified into four stratigraphic units (Figure 6).

A significant layer of the Pabdeh Formation in the Zagros area is thought to be a thin bedded purple shale that is about 2 meters thick and is found in the bottom lithostratigraphical unit above the Gurpi Formation. Limestone with thin to medium bedded limestone characterizes the second stratigraphic block, which is 95 m thick. Dark grey shale, grey marls, and thin bedded limestone alternately layer to make up the third stratigraphic unit, which is 98 m thick. Greenish grey marl predominates in the fourth unit of the formation (57 m thick), with intercalations of thin to medium bedded beige to yellow pelagic limestone. This is the formation's highest point. The Asmari Formation's top lithostratigraphic border is in a transitional state.

Limestone that has been phosphatized makes up the phosphatic horizon, which is 5 m thick and situated 127 m from the section's bottom (in the third stratigraphic unit). Shell-lags, hummocky cross stratification, and ripple marks on the top of the beds were among the sedimentological features that field investigations revealed on these phosphatic layers. The phosphatic horizon has a 5% P2O5 average grade.

3. Components and procedure

The sections underwent systematic sampling to look at the lithological variance. For petrographic research, 487 thin slices from the materials were created (191 from the Nill, 170 from the Mondun and 126 from the Siah sections). The petrographic research (microfacies description) and field observations served as the foundation for the facies analysis (lithofacies description). In the field, researchers looked at the geometry of the sedimentary formations, depositional textures, grain size, macrofaunal and trace fossil richness, stratal surfaces, and facies stacking patterns. In petrographic research, the lithology, depositional texture, diagenesis, and microfossil content were examined. 37 samples were collected from the phosphate horizons. At Kansaran Binaloud

Co., major and trace elements from entire rock studies were studied (Tehran, Iran). By using Inductively Coupled Plasma - Atomic Emission Spectrometry (ICP-AES) analysis, major-element measurements for SiO2, TiO2, Al2O3, Fe2O3 (T), MnO, MgO, CaO, Na2O, K2O, and P2O5 were made. By analyzing the fusion solutions using ICP-mass spectrometry (ICP-MS), more TEs (Hf, Mo, Nb, Rb, Th, U) and rare-earth elements (REEs) La, Ce, Pr, Nd, Sm, Eu, Gd, Tb, Dy, Ho, Er, Tm, Yb, Lu were discovered. Detection limits were 0.01% for all the key elements except MnO and TiO2, for which the limits were 0.001%. Sc, Th, U, Hf, Sb, 0.2, As, Br, Cd, 0.5, Cu, Nb, Ni, Zn, 1; Mo, Rb, Sr, Y, 2; Ba, 3; Zr, 4; and Cr, V, 5 were the detection limits (ppm) for the TEs. The following REEs have detection limits (ppm): La, Ce, Nd, Sm, Gd, Tb, Dy, Ho, Er, Yb, 0.1; Eu, Tm, 0.05; and Lu, 0.04. The XRD analysis was implemented at Kansaran Binaloud Co (Tehran, Iran).

Detailed palaeontological studies and biostratigraphic analysis of the samples were carried out using the biozonation model proposed by Wade et al. [58]. Dunham [59], Wilson [22], and Flugel [60] served as the foundation for the carbonates' microfacies categorization.

4. Results

4.1. Petrography and mineralogy

4. Results

Calcite, quartz, pyrite, and orthoclase are the gangue minerals, according to petrographic examinations carried out using a Zeiss Axioplan 2 Polarized Light Microscope (Islamic Azad University, Science and Research branch, Tehran, Iran). A wide range of skeletal and non-skeletal grains, calcite cements, and micrite make up the Pabdeh Formation. Across the three research regions, there are variations in the quantity of allochems.

The Mondun anticline is rich in non-skeletal grains, the majority of which are ooids, intraclasts, and peloids (Figure 8). Ooids' nuclei are frequently peloids, and occasionally they include foraminiferal tests. All samples of the Nill, Mondun, and Siah anticlines include intraclasts. Phosphate makes up the majority of intraclasts, however some also contain peloids and bioclasts.

4. Results

Peloids are identifiable in all sections, although the Mondun anticline has a greater number of them than the Nill and Siah anticlines. Most pellets in the phosphatized horizons of the Mondun section are consistent in size, tiny, comparable in size, well-sorted, homogeneous in shape, and orange in color. Crinoids, bryozoas, ostracoda, and several planktonic and benthic foraminifera make up the majority of skeletal grains. Heterolepa sp., Haplophragmium sp., Elphidium sp., Reusella sp., Nephrolepidina sp., Pseudolituonella reichelli, and Pyrgo sp. are benthic foraminifera, as are Acarinina sp., Morozovela sp., Globigerinatheka sp (see Supplementary).

Calcite cementation of the intergranular region inside the phosphatic and non-phosphatic grains varies (as a micrite, microsparite and rarely sparite). They might possibly be replaced by phosphatic grains in phosphatized horizons. Petrographic studies reveal similarities between the phosphatic components of the Pabdeh Formation and those of other deposits (pellets, phosphatized intraclasts, ooids, bioclasts, including bone and teeth), but they also show distinct variation in the non-phosphatic components (quartz, glauconite, lithoclasts, calcitic bioclasts, and microcrystalline aggregates of carbonate minerals). Calcite predominates among the nonphosphatic components in phosphorites from the Pabdeh Formation. Glauconite and

sulphides (pyrite) are examples of accessory minerals that can be found in certain beds.

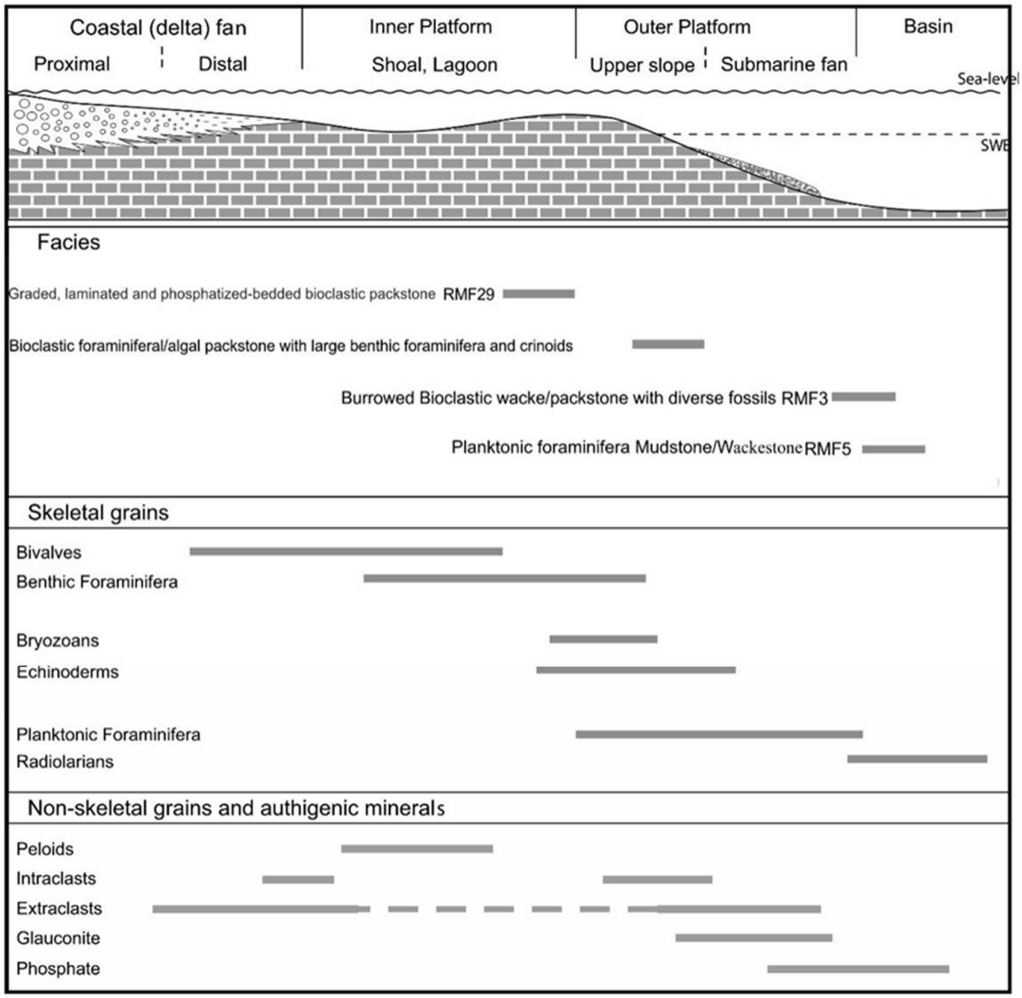

Figure 8. Pabdeh Formation's depositional environment is shown in a schematic cross-section. The lateral distributions of depositional facies and grain associations, the primary energy levels, and the depositional environments (skeletal and non- skeletal). Inspired by [61].

Figure 9's XRD study findings show that fluorapatite makes up the majority of the phosphatic ore minerals in the Pabdeh Formation, whereas the related gangue minerals include calcite, quartz, clay minerals (kaolinite, illite), pyrite, and feldspars (orthoclase and albite).

Table 1 shows the findings from the XRD study, and Table 2 shows the findings from the major-element XRF investigation. The tabulated data make it clear that the phosphate deposits, with an initial P2O5 grade of 8–10%, are of extremely low quality and may be classified as sedimentary phosphate ore with carbonate gangue given the high CaO concentration.

Table 1. X-ray diffraction (XRD) analysis of a representative phosphate ore sample from the Siah anticline.

Mineral type	Calcite	Quartz	Kaolinit	Illite	Fluorapatite	Other minerals	Total
%	67	6	5	2	18	2	100

Table 2. Major element geochemical analysis of a representative phosphate ore sample from the

Content	SiO_2	Al_2O_3	Fe_2O_3	CaO	Na_2O	K_2O	MgO	TiO_2	MnO	P_2O_5	S	L.O.I	Other	Total

%	9.24	2.45	1.67	46.01	0.28	0.38	0.72	0.102	0.012	9.164	0.003	28.98	0.989	100

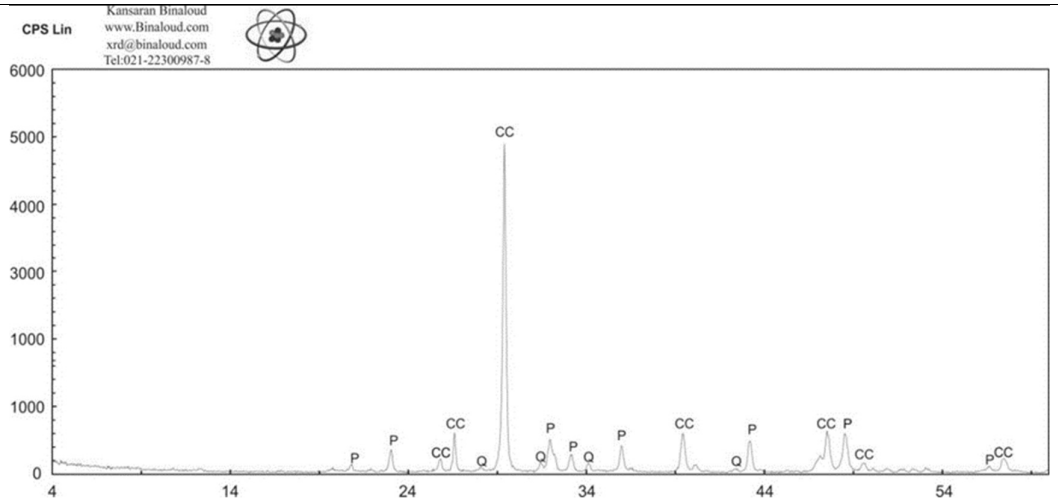

Figure 9. X-ray diffraction patterns Siah anticline phosphorite sample. P: apatite, CC: calcite, Q: quartz. Apatite and calcite are the major minerals.

4.2. Geochemistry

Because of its commercial significance, phosphorites and their constituent apatite are investigated all over the globe [62], and in particular, the geochemistry of phosphorites is utilized to estimate paleo-marine geochemistry [63].

Since apatite substitutes REE3+ and Y3+ for Ca2+, phosphorite often includes significant amounts of trace elements, REE, and yttrium (Y) compared to typical shale and other sedimentary rocks [62,64–67]. In the current investigation, shales and phosphatic strata (Grey columns) were analyzed for main elements, trace elements, and REY. The findings are shown in Table 3.

4.2.1. Major elements

CaO, SiO2, and P2O5 make up the majority of the main oxides in the phosphate-bearing layers, with Al2O3 and Fe2O3 (T) being the next most common components. All other oxides, including MgO, Na2O, SO3, MnO, K2O, and TiO2, have relatively low amounts (less than 1%). P2O5 values (20–25%) from samples from the Mondun section had the highest levels (Table 3). When fluorapatite is assumed to have an average P2O5 concentration of 23%, sediments from the Siah and Nill Basins and the Mondun Basin have an average fluorapatite content of 81% and 38%, respectively.

The high CaO (32.45–48.65%) and extremely low MgO (0.4–1.09%) compositions of the samples from all three sections reflect the large amounts of calcite and suggest that Mg may not have been included in the apatite structure. CaO is present with an average concentration of 40.43%. P2O5 and CaO show a weak connection (R2 = 0.014). The SiO2 values vary significantly, from 6.37% to 31.35%, reflecting the shifting amount of quartz (from detrital and biogenic sources) [68]. As TiO2 has an R2 value of 0.47 and exhibits a rather high positive connection with Al2O3, the TiO2 values, which range from 0.004% to 0.19%, are thought to mostly reflect clay minerals. Significant range in the Al2O3 contents (0.69–5.52%) is seen in the deposits and is due to the occurrence of clay mineral assemblages.

Na2O and K2O, the two alkali components, vary somewhat (0.01% to 0.27% and 0.27% to 1.05%, respectively). Na and K substitution in the feldspar components may explain the very poor link between Na2O and P2O5 (R2 = 0.019) and the negative relationship between K2O and

P2O5 (R2 = 0.053). The kind and quantity of illite, glauconite, and K-feldspar in the assemblage essentially influence the K2O concentration. Fe2O3 concentration varies between 0.86% and 3.75%. The carbonate nature of the mineralized and non-mineralized strata is the cause of the low Fe2O3 readings. The SO3 level ranges from 0.002% to 0.41%, which may be attributed to the existence of sulphides and the presence of sulphate as a component element [67,69]. (pyrite). [70].

4.2.2. Trace elements

It is well acknowledged that the phosphorite facies is characterized by an enhanced trace element group made up of Sc, Mo, Zn, Cd, Ag, U, Y, and REEs [67,71–73].

Sr (1222.9 ppm), Cr (142.4 ppm), Ba (138.6 ppm), Zn (71.1 ppm), V (66.8 ppm), Ni (59.8 ppm), Cu (22.9 ppm), Mo (11.4 ppm), Zr (10.5 ppm), U (7 ppm), Th (6.8 ppm), As (6.6 ppm), Sc (4.5 ppm), and Sb are the average trace element concentrations ((1 ppm). The distribution of trace elements in phosphorite horizons may be divided into three groups based on the element concentrations: The first group included rather high quantities (140 ppm) of Cr and Ba.

The second category consists of Mo, Ni, Zn, V, Zr, and Cu in moderate quantities (10 to 70 ppm) of TEs. U, Th, Sc, As, and Sb are among the TEs in the third group, which are present in relatively low amounts (10 ppm).

Traces of elements

There is considerable and traces element fractionation as compared to the Post Archean AustralianShale normalized (PAAS) (Figure 10a–c). SiO2, Al2O3, CaO, P2O5, Sr, Cd, Zn, Cr, Cu, Ni, Zr, Ba, Rb, Th, As, and Sc concentrations are more than PAAS for values greater than 1. If the numbers are negative one, the PAAS's compositional deficiency is present (Na2O, TiO2 and Fe2O3). Values for MgO and Sb are comparable to PAAS.

The research region's phosphorites have a range of 486 to 2075 ppm strontium content. Because Sr and P2O5 have a strong association (R2 = 0.79), it is clear that Sr is part of the fluorapatite structure. These phosphorites' comparatively high Sr concentrations may be the product of replacements for Ca in fluorapatite [67]. These phosphorites contain chromium in concentrations ranging from 23 to 370 ppm, with an average of 138.6 ppm. It is clear from the positive connection between Cr and P2O5 (R2 = 0.81) that Cr may have a role in apatite structure.

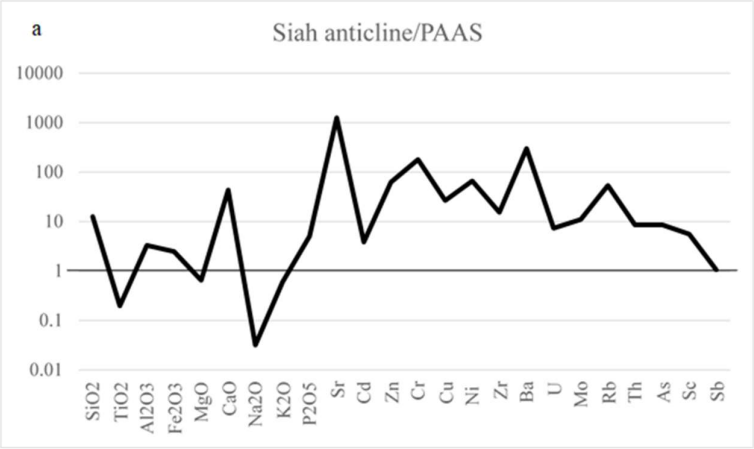

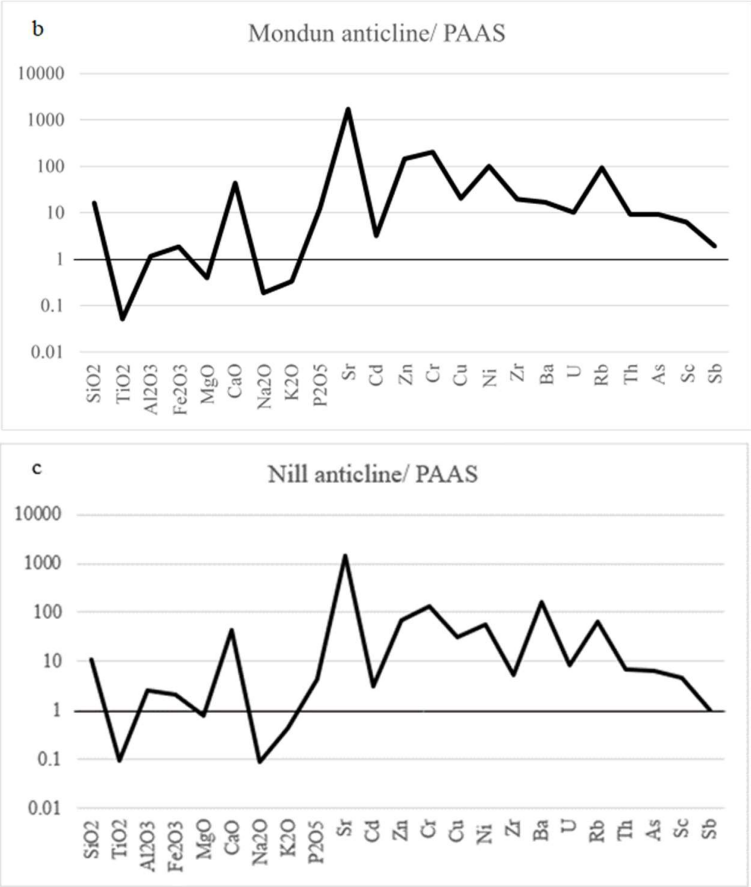

Figure 10. (a), (b), (c). Shale normalized (PAAS) averages major and trace elements spectra of phosphatic samples from Siah, Mondun and Nill sections.

Table 3a. Concentration of major elements (wt%), trace elements (ppm), rare earth elements (ppm), and elemental ratios in 14 phosphatic and non phosphatic samples from the Siah anticline.

Locality	Siah section							Phosphatic layers						
Sample No	N129	N130	N131	N132	N133	N134	N135	N136	N137	N138	N139	N140	N141	N142
Major Oxides%														
SiO_2	18.65	14.85	14.7	6.37	15.43	8.97	11.32	17	12.7	17.7	7.65	31	10.52	7.45
TiO_2	0.2	0.17	0.19	0.06	0.223	0.12	0.15	0.52	0.07	0.25	0.08	0.2	0.14	0.09
Al_2O_3	3.63	3.65	3.8	1.47	4.85	2.57	3.74	3.85	1.85	5.52	2.11	3	2.99	1.89
MnO	0.001	0.004	0.01	0	0.021	0.04	0.05	0	0	0.01	0	0	0.02	0.01
MgO	0.7	0.55	0.64	0.54	0.65	0.64	0.65	0.52	0.43	0.89	0.75	0.9	0.59	0.46
CaO	39.45	41.96	41.9	49.7	39.61	44.62	43.65	41.7	43.7	37.5	48.4	32	45.26	48.7
Na_2O	0.27	0.03	0.04	0.01	0.04	0.02	0.02	0.06	0.04	0.03	0.02	0.2	0.06	0.02
K_2O	0.81	0.68	0.78	0.31	0.77	0.55	0.7	0.62	0.37	1.05	0.29	0.6	0.54	0.35
P_2O_5	0.59	0.79	0.48	0.45	0.60	2.95	3.3	8.24	8.65	4.1	2.99	0.4	0.38	0.14

					8									
SO_3	0.002	0.013	0.06	0.03	0.012	0.06	0.1	0.36	0.12	0.2	0.01	0.3	0.03	0.01
L.O.I	33.02	33.66	34.9	39.6	32.33	36.67	33.14	24.2	28.7	29	36	28	37.6	39.7
Fe_2O_3	2.34	1.79	2.36	1.18	3.53	2.3	2.77	2.37	2.46	3.75	1.14	2.6	1.51	0.86
Total	99.663	98.15	99.7	99.6	98.07	99.51	99.59	99.4	99	100	99.4	100	99.64	99.6
TE (ppm)														
As	2.7	2.5	2.8	2	2.9	7.5	6.9	11.2	9.4	9.1	7.4	2.6	2.3	2.1
Ba	114	160	371	33	86	325	707	123	156	168	311	360	131	156
Cd	1	2.3	0.3	0.8	5	7.1	0.31	1.5	3.4	3.8	6.9	0.3	2.6	0.4
Cr	39	52	74	23	127	189	152	247	142	166	178	75	43	46
Cu	21	18	14	10	24	29	26	23	22	32	27	16	17	21
Mo	1.65	6.5	7.8	1.56	9.9	13.2	6	14	9.6	10.1	12.9	11	9.1	2.5
Ni	22	35	47	25	74	84	50	67	52	57	86	49	28	39
Sb	1.02	1.11	1.01	1.01	0.94	0.99	0.87	0.99	1.16	1.3	0.98	1	1.3	0.83
Sc	2.2	2.8	3.2	1.4	4.6	5.6	4.8	6.7	4.9	5.8	5.4	3.3	3.5	3.1
Sr	660	595	581	645	1032	1026	1060	1441	1325	1600	1033	592	486	536

Locality	Siah section					Phosphatic layers								
Sample No	N129	N130	N131	N132	N133	N134	N135	N136	N137	N138	N139	N140	N141	N142
TE (ppm)														
Th	6.6	7.6	8.2	6.6	7.3	8.1	10.4	8.7	7.8	8.1	8.2	7.9	5.4	6.8
U	4.9	3.9	4.2	3.2	4.5	5.8	6.3	9.1	7.6	9.3	5.6	4.1	3.5	3.3
V	28	80	38	25	103	104	53	85	65	77	107	37	59	65
Rb	17	6	11	4	17	28	50	73	60	80	30	9	8	16
Zn	46	54	35	37	33	43	53	51	90	92	44	32	47	57
Zr	12	16	20	8	10	21	17	16	8	7	23	27	13	14
REE (PPM)														
La	8.53	9.2	4.8	7.73	6.5	17.72	22.43	31.1	33.2	26.7	20.2	6.6	4.42	4.59
Ce	17.14	11.4	7.17	14.3	7.36	23.09	30.49	37.2	37.5	32.3	26.7	7.1	6.29	6.7
Pr	2.08	2.14	1.78	1.58	1.1	2.19	2.82	5.21	5.24	3.01	1.98	1.5	0.96	0.99
Nd	5.32	6.21	3.5	4.3	4.1	19.07	24.77	28.7	29.1	25.4	21.7	4	3.22	3.01
Sm	1.32	0.92	0.73	1.29	0.71	1.11	1.28	4.04	4.3	1.99	2.09	1.6	0.59	0.51
Eu	0.3	0.2	0.1	0.2	0.1	0.28	0.49	0.97	0.99	0.65	0.42	0.2	0.1	0.1

	9	2	8	5	5								2	
Gd	1.42	0.91	0.61	1.21	0.68	1.21	2.37	4.62	4.98	2.51	3.06	0.7	0.57	0.47
Tb	0.17	0.22	0.15	0.13	0.15	0.21	0.41	0.87	0.93	0.5	0.37	0.1	0.13	0.14
Dy	0.93	1.14	0.64	0.93	0.82	2.22	3.2	5.61	5.86	3.49	2.87	0.8	0.72	0.53
Ho	0.26	0.29	0.2	0.19	0.19	0.41	0.9	1.29	1.4	0.91	0.69	0.2	0.15	0.13
Er	0.72	0.72	0.44	0.67	0.6	1.93	1.5	3.99	4.5	1.84	2.32	0.6	0.44	0.39
Tm	0.14	0.11	0.08	0.13	0.1	0.12	0.16	0.59	0.69	0.22	0.19	0.2	0.05	0.03
Yb	0.79	0.94	0.47	0.56	0.59	1.62	1.99	3.41	3.75	1.27	2.05	0.6	0.46	0.47
Lu	0.16	0.12	0.07	0.14	0.11	0.19	0.2	0.58	0.62	0.25	0.18	0.1	0.07	0.04
Y	6.96	9.96	6.67	6.4	7.65	37.87	52.48	59.9	61.1	52.3	45.6	7.2	5.99	4.73
∑REE	39.37	34.54	20.8	33.4	23.16	71.37	93.01	128	133	101	84.8	24	18.19	18.1
∑REE_Y	46.33	44.5	27.5	39.8	30.81	109.2	145.5	188	194	153	130	31	24.18	22.8
Ce/Ce*	1.065	0.627	0.733	0.956	0.6	0.565	0.587	0.547	0.529	0.543	0.577	0.559	0.714	0.714
La/Nd	1.603	1.481	1.37	1.8	1.585	0.929	0.906	1.08	1.14	1.05	0.93	1.7	1.373	1.52

Table 3b. Concentration of major elements (wt%), trace elements (ppm), rare earth elements (ppm), and elemental ratios in 14 phosphatic and non phosphatic samples from the Mondun anticline.

Locality	Mondun section													
Sample No	N69	N70	N71	N82	N83	N84	N88	N89	N90	N91	N92	N149	N150	N151
Major Oxides%														
SiO_2	13.83	16.51	16.38	15.88	19.38	13.78	14.38	11.85	14.56	16.64	14.54	13.62	19.17	14.54
TiO_2	0.035	0.052	0.01	0.036	0.08	0.079	0.024	0.036	0.026	0.033	0.004	0.041	0.063	0.004
Al_2O_3	1.66	1.13	2.37	3.1	1.6	1.64	1.88	0.69	0.95	2.62	1.82	1.61	1.41	1.98
MnO	0.007	0.002	0.003	0.006	0.001	0.063	0.004	0.001	0.002	0.0023	0.007	0.0055	0.001	0.0019

MgO	0.45	0.4	0.42	0.55	0.45	0.83	0.57	0.37	0.35	0.52	0.57	0.39	0.41	0.36
CaO	45.59	43.31	43.96	40.85	41.19	45.57	46.22	46.75	45.02	44.69	45.19	44.93	41.25	44.61
Na_2O	0.08	0.22	0.04	0.031	0.21	0.11	0.2	0.15	0.18	0.22	0.19	0.12	0.18	0.19
K_2O	0.33	0.28	0.45	0.72	0.36	0.27	0.51	0.38	0.34	0.47	0.41	0.41	0.3	0.41
P_2O_5	0.52	5.51	0.36	0.41	5.08	0.39	0.49	25.12	22.32	0.36	0.32	0.71	4.12	0.58
SO_3	0.29	0.06	0.43	0.02	0.12	0.09	0.35	0.22	0.27	0.23	0.16	0.25	0.03	0.18
L.O.I	34.29	30.47	33.4	35.71	29.02	35.06	33.52	11.93	13.97	32.49	33.95	35.44	30.89	34.57
Fe_2O_3	2.41	1.8	1.68	2.29	2.06	1.53	1.53	2.15	1.65	1.11	2.36	1.78	1.61	2.05
Total	99.492	99.74	99.5	99.6	99.551	99.412	99.68	99.647	99.638	99.385	99.52	99.307	99.434	99.476
TE (ppm)														
As	2.3	9.2	3.46	3.81	4.3	4.26	5.01	15.1	13.8	5.08	6.55	5.39	3.9	4.62
Ba	53	7	44	37	2	60	47	38	34	67	73	59	3	64
Cd	0.91	1.2	1.8	0.73	1.1	2.59	0.73	6.78	5.98	1.36	1.11	0.97	0.9	1.42
Cr	35	95	46	70	95	52	56	370	349	61.1	54	76	101	75.8
Cu	13	7	16	11	10	22	13	37	32	15	22	12	16	26
Mo	3.38	13.3	2.95	6.63	15.6	2.95	6.63	33	36	5.59	4.28	3.74	14.2	4.69
Ni	39	73	35	41	82	51	38	134	140	39	45	41	74	37
Sb	1.49	0.95	1.09	1.36	0.89	0.94	1.26	3.6	3.2	0.87	1.21	0.91	0.91	1.34
Sc	2.2	5.1	2.35	3.11	4.3	4.22	3.61	9.1	8.1	2.41	3.04	2.73	4.7	2.66
Sr	747	1503	690	587	1456	836	903	2075	1974	710	660	580	1499	690

Locality	Mondun section													
Sample No	N69	N70	N71	N82	N83	N84	N88	N89	N90	N91	N92	N149	N150	N151
TE (ppm)														
Th	5.5	7.1	6.65	8.1	7.4	5.26	6.32	13.2	11.9	4.95	7.35	5.63	6.8	6.41
U	4.42	8.5	3.98	4.36	7.9	3.21	3.69	12.8	13.2	3.33	4.01	3.69	8.3	2.97
V	31	73	49	36	87	27	43	84	78	28	33	19	81	25
Rb	35	61	32	61	59	26	29	148	139	52	77	65	59	59

Zn	57	65	75	67	93	71	47	253	235	61	39	44	77	38
Zr	23	15	20	16	11	17	26	31	25	21	12	30	16	15
REE (ppm)														
La	6.77	26.79	6.85	8.25	24.61	9.94	14.3	32.4	28.4	8.54	10.2	7.91	22.88	8.02
Ce	11.9	34.02	11.3	7.97	33.26	6	10.6	59.5	50.24	5.7	9.93	7.12	34.26	4.97
Pr	2.14	4.33	1.55	2.35	5.02	2.3	4.52	7.76	6.03	2.69	2.36	2.73	4.18	1.92
Nd	5.39	15.38	3.9	4.46	17.77	7.58	7.48	21.8	20.01	2.87	3.58	3.01	16.57	3.02
Sm	1.05	4.53	0.79	0.73	4.61	0.75	1.02	5.49	4.86	0.43	0.81	0.56	4.19	0.55
Eu	0.61	0.99	0.21	0.16	1.13	0.11	0.51	1.23	0.93	0.12	0.36	0.16	1.05	0.14
Gd	1.2	7.1	1.31	0.72	6.86	0.75	1.27	7.41	6.43	0.53	2.36	0.58	6.92	0.67
Tb	0.17	0.78	0.15	0.15	0.91	0.22	0.27	0.99	0.9	0.09	0.34	0.1	0.83	0.1
Dy	0.89	5.41	0.81	0.93	5.95	1.17	1.15	6.58	5.72	0.48	2.01	0.6	4.88	0.55
Ho	0.24	1.22	0.19	0.25	1.37	0.32	0.32	1.67	1.24	0.18	0.54	0.15	1.11	0.26
Er	0.61	3.73	0.55	0.6	4.17	0.74	0.78	4.42	4.09	0.37	1.3	0.4	3.75	0.34
Tm	0.14	0.62	0.17	0.09	0.75	0.13	0.2	1.21	0.73	0.21	0.22	0.09	0.69	0.19
Yb	0.85	4.02	0.78	0.48	3.36	0.84	1.03	4.69	3.57	0.39	1.24	0.3	3.91	0.48
Lu	0.17	0.61	0.14	0.1	0.54	0.13	0.21	0.89	0.8	0.07	0.25	0.06	0.58	0.09
Y	8.44	57.7	7.99	8.63	60.48	11.2	9.12	73.6	66.9	4.56	14.38	5.53	56.34	5.04
∑REE	32.13	109.5	28.7	27.24	110.31	30.98	43.66	156.04	133.95	22.67	35.5	23.77	105.8	21.3
∑REE_Y	40.57	167.2	36.69	35.87	170.79	42.18	52.78	229.64	200.85	27.23	49.88	29.3	162.14	26.34
Ce/Ce*	0.850	0.670	0.885	0.493	0.672	0.284	0.408	0.93	0.876	0.3	0.173	0.24	0.75	0.363
La/Nd	1.25603	1.742	1.756	1.85	1.38449	1.31113	1.912	1.48062	1.41993	2.97056	2.849	2.62779	1.38008	2.65056

Table 3c. Concentration of major elements (wt%), trace elements (ppm), rare earth elements (ppm), and elemental ratios in 9 phosphatic and non phosphatic samples from the Nill anticline.

Locality	Nill Section								
Sample No	N12	N15	N18	N55	N56	N57	N58	N61	N63
Major Oxides%									
SiO_2	12.33	12.97	13.05	11.52	12.65	13.45	10.45	7.65	12.64
TiO_2	0.14	0.15	0.083	0.081	0.067	0.062	0.094	0.075	0.098
Al_2O_3	2.78	3.72	2.54	3.04	1.85	1.23	2.39	2.11	1.94
MnO	0.004	0.03	0.003	0.004	0.002	0.0032	0.015	0.001	0.005
MgO	0.67	1.09	0.71	0.61	0.43	0.58	0.88	0.75	0.64
CaO	42.31	42.68	44.02	42.26	43.68	42.97	44.78	48.37	43.54
Na_2O	0.06	0.2	0.07	0.04	0.04	0.14	0.06	0.02	0.087
K_2O	0.69	0.67	0.52	0.51	0.37	0.49	0.41	0.29	0.49

P_2O_5	0.3	2.01	0.32	0.62	8.65	0.53	0.62	1.98	0.36
SO_3	0.21	0.16	0.009	0.003	0.12	0.01	0.004	0.005	0.06
L.O.I	37.66	33.54	35.47	38.9	28.65	38.44	38.79	36.82	36.39
Fe_2O_3	2.04	2.63	2.55	1.71	2.46	1.41	1.09	1.14	2.95
Total	99.194	99.85	99.345	99.298	98.969	99.3152	99.583	99.211	99.2
TE (ppm)									
As	2.48	4.9	2.65	2.45	9.1	1.71	2.39	4.71	2.3
Ba	151.3	181	137	163	168	103	133	155	115
Cd	1.88	2.89	1.56	1.3	3.8	0.94	1.21	2.62	1.32
Cr	47.3	131	45.5	48.4	166	39.74	48.37	111	35.32
Cu	17.3	35	19.5	12	32	13	15.23	26	15.6
Mo	5.58	10.1	4.07	4.62	13.33	5.78	5.57	9.25	5.59
Ni	41.2	57	28.5	45	61	31	39.28	55	43
Sb	1.04	0.93	1.04	0.98	1.3	1.2	1.05	0.82	1.05
Sc	2.86	4.87	2.78	3.06	5.8	3.04	2.99	3.11	3.01
Sr	620	1507	612	607	1600	487	578	1321	562

Locality	Nill Section								
Sample No	N12	N15	N18	N55	N56	N57	N58	N61	N63
TE (ppm)									
Th	7.27	6.44	7.4	6.9	8.1	5.23	6.93	6.13	6.6
U	4.16	8.71	4.02	3.96	9.3	3.16	3.88	6.54	3.79
V	42.35	77	48	53	83	35.67	43.54	62	44.23
Rb	9	59	11.3	10.2	80	8.2	9.88	50	9.6
Zn	41	77	35	45	92	51	41.66	44	43
Zr	13	5	12	9	7	15	11	4	13
REE (ppm)									
La	7.34	20.07	5.21	6.19	26.7	4.65	6.12	17.11	4.81
Ce	11.45	26.69	6.7	13.27	32.31	7.89	10.77	21.45	8.22
Pr	1.73	2.53	1.13	1.42	3.01	1.11	1.49	2.06	1.51
Nd	4.25	21.92	3.4	4.1	25.43	4.21	4.28	19.18	4.42
Sm	0.99	1.19	0.89	1.29	1.99	0.59	0.98	1.12	0.85
Eu	0.22	0.55	0.14	0.32	0.65	0.12	0.24	0.43	0.25
Gd	0.93	1.94	0.58	0.73	2.51	0.57	0.81	1.08	0.64
Tb	0.16	0.42	0.13	0.14	0.5	0.09	0.14	0.31	0.17
Dy	0.89	2.88	0.71	0.77	3.49	0.39	0.69	2.31	0.49
Ho	0.22	0.73	0.15	0.19	0.91	0.13	0.17	0.67	0.18
Er	0.66	1.72	0.49	0.52	1.84	0.32	0.51	1.7	0.37
Tm	0.1	0.17	0.08	0.13	0.22	0.05	0.09	0.13	0.04
Yb	0.51	1.8	0.47	0.43	1.27	0.4	0.49	1.17	0.39
Lu	0.12	0.19	0.07	0.05	0.25	0.08	0.1	0.13	0.14
Y	7.42	41.47	5.97	7.04	52.3	4.43	6.12	32.8	4.93
∑REE	29.57	82.8	20.15	33.41	101.08	20.6	26.88	68.85	22.48
∑REE_Y	36.99	124.27	26.12	39.81	153.38	25.03	33	101.65	27.41
Ce/Ce*	0.843	0.577	0.638	1.086	0.543	0.75	0.910	0.542	0.795
La/Nd	1.727059	0.9156	1.5324	1.7977	1.0499	1.10451	1.42991	0.8921	1.0882

According to Prevot and Lucas [74], Cr is primarily removed by apatite and is stable in clays, so it can be assumed that during the precipitation of phosphatic ores, chromium concentration was stable in the clay and ironiferous minerals, explaining the relatively high concentration of Cr found in phosphorites. These phosphorites contain Zn in concentrations ranging from 23 to 253 ppm, with an average of 71.1 ppm. The abundance of pyrite and organic materials in Mondun phosphorites may be the cause of their high Zn content. These phosphorites contain trace amounts of uranium, with a concentration range of 2.97 to 13.2 ppm and an average of 5.43 ppm (Table 3). The apatite lattice is thought to accommodate this element very easily [71,75,76]. According to this study's positive correlation between U and P2O5 (R2 = 0.77), the apatite phase in phosphorites is where the majority of the uranium is found [71,77–82]. As zirconium and P2O5 have a weakly positive connection (R2 = 0.086), apatite does not contain zirconium. These phosphorites have an average Ni concentration of 51.57 ppm and a range of 22 to 140 ppm. Ni and P2O5 have a positive association (R2 = 0.73), which suggests that a significant quantity of Ni may be found in the apatite lattice [83,84]. Individual Mondun phosphatic horizons had the greatest concentrations of Sr, Zn, Y, Ni, and U, whereas Nill and Siah phosphatic horizons had the largest concentrations of Ba.

Ba content in this experiment ranged from 2 to 707. It should be noted that the restricted Ca substitution by Ba is suggested by the negative association of P2O5 with Ba. Ba cannot replace Ca in the fluorapatite lattice as Sr can, despite the fact that Ba and Sr exhibit the same geochemical behavior due to the greater ionic radii [52]. The presence of barite occurrences in the depositional region is a significant potential cause of the increased concentration of Ba in the Siah section [52].

Although in this instance certain Mondun non-phosphatic sediment samples show very modest increases in TE contents, similar patterns are not visible in the bulk non-phosphatic layers (Table 3).

Due to the high glauconite composition of the sediments, phosphorites from Mondun have the greatest As and Sb contents [85,86]. The range of thorium concentration is 4.95 to 13.2 ppm. The samples from the phosphorite beds of the Mondun region are characterized by high Th levels. Due to their similar ionic radii, this element can take the place of Ca in the fluorapatite lattice.

The levels of cadmium in the Pabdeh phosphatic layers vary, and in certain samples from the Siah section, the level is 7.1 ppm (>1.1 average shale).

4.2.3. Rare-earth elements and yttrium

Rare earth elements have been employed as tools for identifying depositional environmental systems, including broad marine anoxia [87–89], lithology and diagenesis [90–93], oceanic palaeo-redox conditions [94,95], and paleogeography and depositional models [96–97]. As REEs are difficult to fractionate during sedimentation, their patterns may hold the key to understanding average provenance compositions [98]. Weathering, burial diagenesis, and metamorphic processes may have an impact on the distribution pattern and concentration of REEs in phosphorites [99]. Recent research on marine phosphorite deposits has shown that phosphorite formation in oceanic sediments may contain a lot of rare earth elements, resulting in extremely early diagenesis [100].

Since REE+Y are easily incorporated into the apatite structure during early diagenesis directly from seawater [67,99,104], it has been known for more than a century that phosphorite layers

contain more REEs than other sedimentary rocks [101–103]. For instance, the amount of REE+Y in fish debris apatite in slowly accumulating current deep-sea muds may exceed 3% ∑REE+Y [105].

In this work, the phosphorite REE was normalized using Taylor & McLennan's Post-Archean Australian Shale normalized (PAAS) [106].

Table 3 lists the elemental ratios and REE+Y concentrations (ppm). In typical shale versus phosphorite layers, the total REE (∑REE) and Y concentrations vary from 27.1 to 103 and 7 to 52.2 ppm, respectively.

Samples from the Mondun section exhibit greater REE levels than those from the Siah (84.8 to 133 ppm, average 101.9 ppm) and Nill (68.8 to 101 ppm, average 84.2 ppm) sections (REE range: 105.8 to 156.4 ppm, average 123.1 ppm). These values are similar to the P2O5 levels in the samples from Mondun. The Siah phosphate deposits have the lowest REE values, with an average of 84.2 ppm (Figure 11).

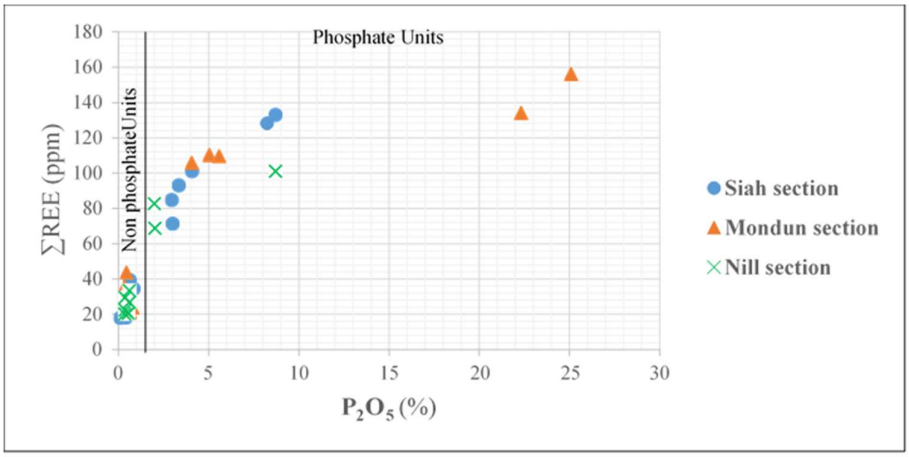

Figure 11. Total rare-earth elements (REE, ppm) in Mondun, Nill, and Siah phosphate and non-phosphate units are shown in a bivariate manner against P2O5 (wt%) concentration.

Hence, it appears that there is rivalry among the REE for space in the apatite lattice. The negative LREE (La, Ce, Pr, Nd) and enrichment in the medium REE (MREE) and heavy REE are characteristics of the shale normalized (PAAS) REE patterns of Mondun phosphorites (Figure 12c,d) (HREE).

The Nill sector records the lowest REE values, which are associated with low grade phosphate levels (P2O5 <4.5%). The majority of the phosphorite readings in the Nill and Siah portions are similar to, or occasionally lower than, the PAAS (Figure 12a,b,e,f).

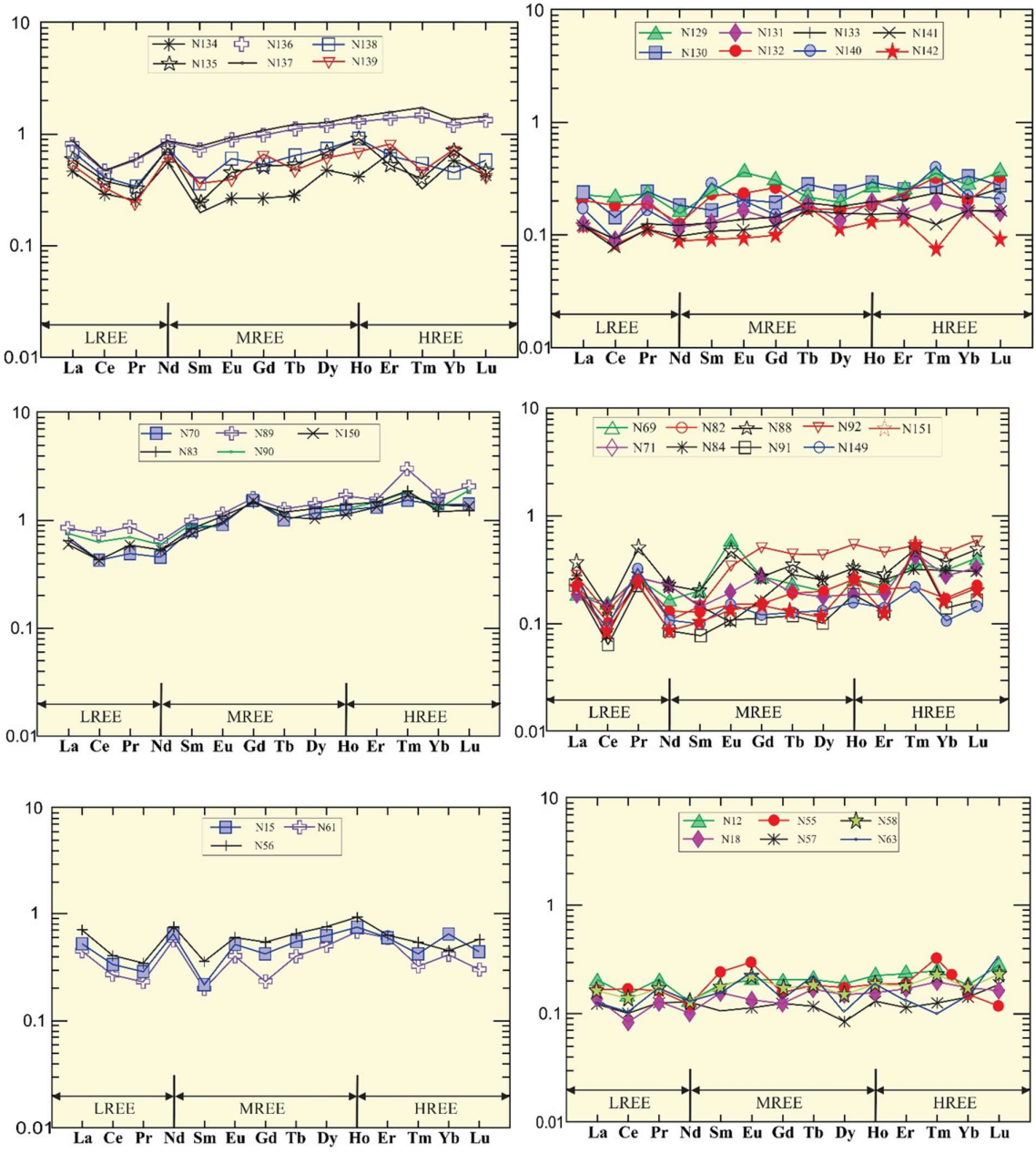

Figure12. a, b, c, d, e, f. Rare earth elements normalized to PAAS (Post Archean Australian Shale, after Taylor and McLennan, [106] of non-phosphatized (a,c,e) and phosphatized (b,d,f) samples of Siah (a,b), Mondun (c-d), and Nill (e,f) sections.

With regard to cerium's REE neighbors lanthanum (La), praesodymium (Pr), or neodymium, shale normalized REE patterns often show a gradual enrichment towards the heavier REE (HREE) and a relative depletion of cerium (Nd). The reduction in solubility associated with the oxidation of cerium (III) to cerium (IV) and subsequent removal of cerium along with other multivalent metals is thought to be the cause of this negative ce anomaly (Ce/Ce*) [107].
Many writers employed the Ce anomaly (Ce/Ce*) [52,108-110]. The Ce anomaly was determined using:
[Ce*=2/3LaN+1/3NdN; Ce/Ce* = 3CeN/ [2LaN+NdN]

where N is the concentrations' normalization for the Shale [88]. Tell people there is no anomaly when Ce anomaly equals 1. It is defined as negative for values less than 1 and as positive for values greater than 1 [52].

These phosphates were generated in suboxic settings that lacked this element, according to samples with negative Ce anomalies [107].

The majority of the phosphorite samples from all three sections are represented in the REE pattern and show highly negative to positive Ce anomalies (values varying between 0.24 and 1.08). Shale adjusted negative Ce anomalies of various magnitudes are evident in all of the examined samples. Together with an HREE enrichment, this anomaly is characteristic of the REE composition of ocean water [111].

Moreover, there are significant positive correlations between REE+Y and Ce anomaly in Mondun Section, whereas in Nill and Siah Sections, the opposite is true (Figure 13a–c) [67,99].

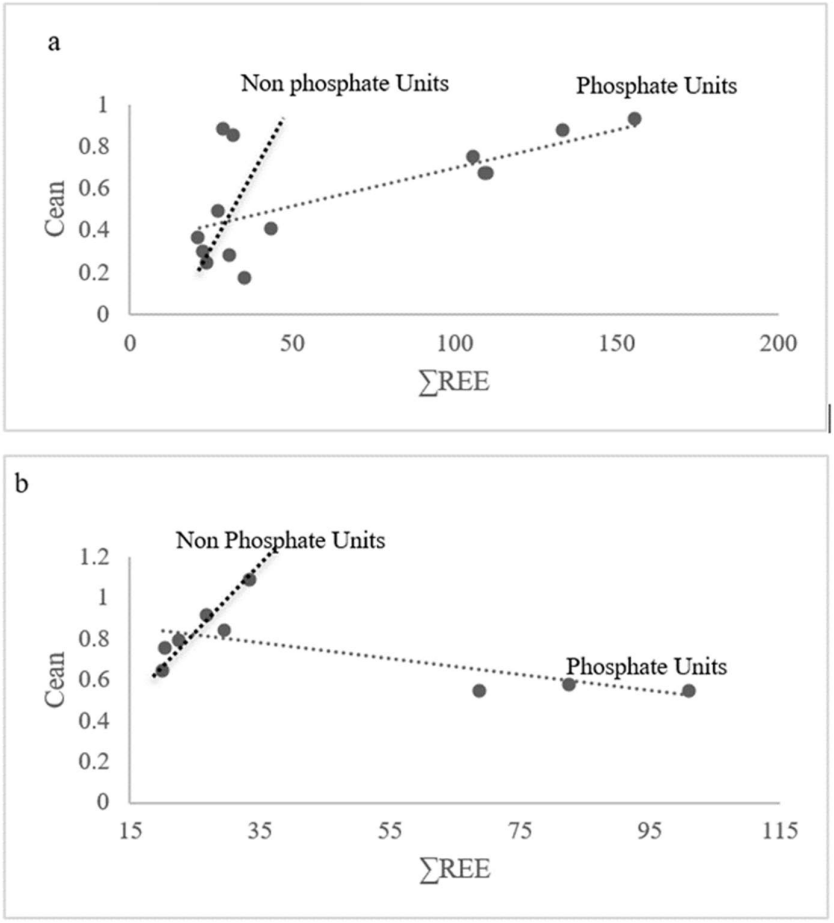

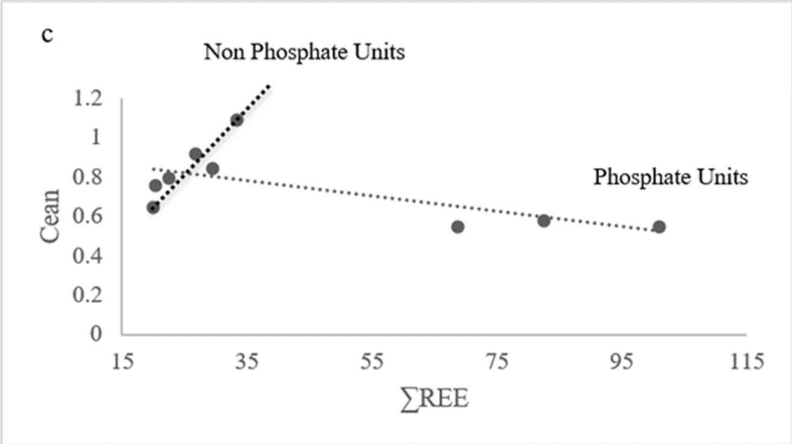

Figure 13. a, b, c. Cean versus ΣREE diagram of samples of Mondun (a), Siah (b) and Nill (c), profile showing positive correlation between the cerium anomaly values and the total REE in Mondun section and negative correlations in Siah and Nill sections.

4.3. Facies analysis

4.3.1. Carbonate facies

In addition to the basal purple shale and thin beds of marl with planktonic forams, such as the Acarininidae, Globigerinidae, Morozovelidae, and Turburotalidae Families and benthic forams, four sedimentary facies were identified in the Pabdeh Formation based on field descriptions and petrographic studies. We discovered shallow water carbonates and marls in the Pabdeh Formation samples, despite the fact that earlier research [3,112] indicated pelagic shales of deep marine settings. The bioclastic mudstone/wackestone, burrowed bioclastic wackestone/packstone, graded, laminated, and phosphatized-bedded bioclastic packstone, and bioclastic foraminiferal/algal/peloidal packstone are the four carbonate facies.

• Wackestone and bioclastic mudstone

These argillaceous limestone and marl intercalations are found in a planktonic and benthic foraminiferal lime mudstone. Morozovellids, Hantkeninids, Pseudohastigerinids, Subbotinids, Turborotalids, Globigerinathekids, Orbulinids, and Globigerinids are a few of the sparse planktonic foraminifera that make up the facies, as well as Elphidium sp., Heterolepa sp., and spora

Limestone, dark grey shale, and grey marls are all examples of bioclastic mudstone/wackestone facies found in the field. Low planktonic foraminiferal content and pyritization suggest that the bioclastic mudstone/wackestone microfacies were deposited below the Fair Weather Wave Base (FWWB), in a deep outer-ramp setting close to the basin edge.

Journal of New Zealand Studies NS35 (2023), https://doi.org/ 10.5281/zenodo.7805493

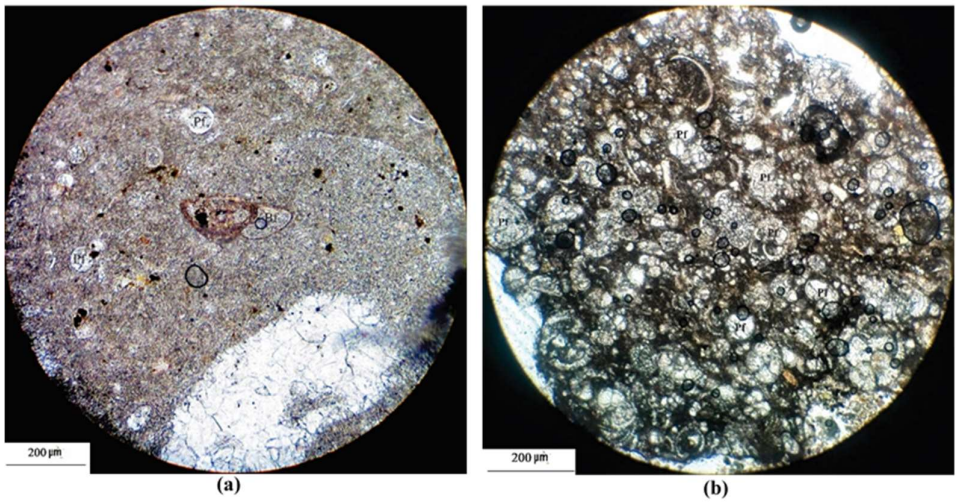

Figure 14. A microphotograph of the bioclastic mudstone to wackestone microfacies is shown in (a). Remarkable benthic foraminifera may be seen. XPL; 200X. (b) Pelagic foraminiferal bioclastic packstone microfacies. XPL; 40X. Foraminifera are classified as either planktonic or benthic.

• Burrowed fossil-rich bioclastic wacke/packstone

This bioclastic wacke/packstone has a wide variety of fossils. Echinoderm and echinoid spines and fragments, as well as scarce pieces of planktonic and benthic foraminifera, make up the allochems. In the bedding planes, burrows both horizontally and vertically are prevalent (Figure 15a,b).

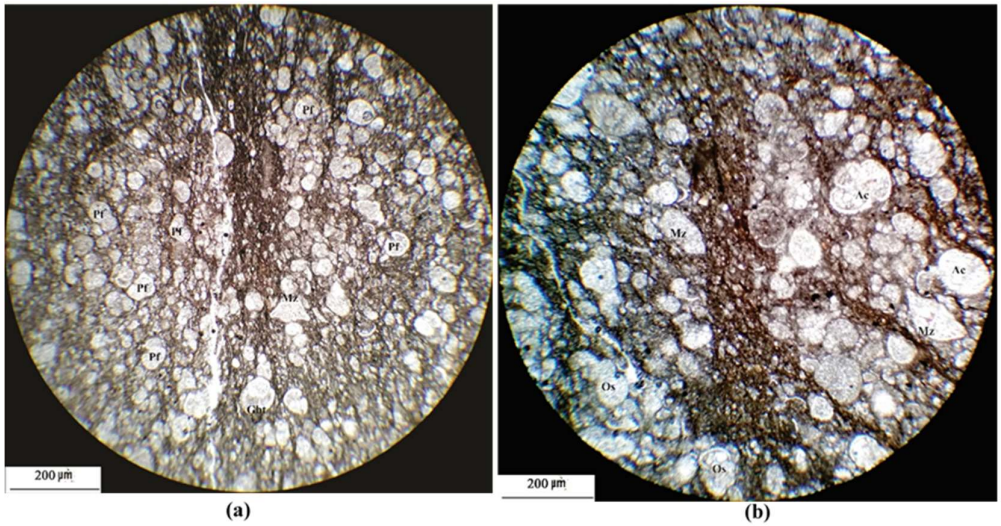

Figure. 15. (a), (b) (b). Burrows developed in a deep marine environment may be seen in the shafts of vertical burrows in microphotographs of burrowed bioclastic planktonic foraminiferal packstone. Pabdeh Formation's lower portion. 200X; XPL. Keep in mind how the micrite chambers were created by excavating the burrows. Foraminiferal abbreviations include Bf (benthic), Pf (planktonic), Ac (acarinina), Mz (morozovella), and Gbt (globigerinatheka).

Journal of New Zealand Studies NS35 (2023), https://doi.org/ 10.5281/zenodo.7805493

Burrowed Below the FWWB, in a deep outer-ramp setting at the margin of the basin, fossil-rich bioclastic wacke/packstone was deposited.

• Bioclastic packstone that has been graded, laminated, and phosphatized-bedded

Interlayered dark mudstones and bioclastic packstone with erosional basal contact, fining-upward succession, and ripple marks on the tops of the beds, comparable to Hips research [30], are characteristics of the microfacies. The prevalence of shell-lag layers, which suggest deposition under sporadic strong storm currents and varied indicators of reworking and movement of sediment from the inner ramp to this location, is another distinctive aspect of the microfacies (Figure 16a). The bioclastic packstone is made up of phosphatic intraclasts, phosphatized foraminifera, and fossilized fish scales and bones (Figure 16b,c).

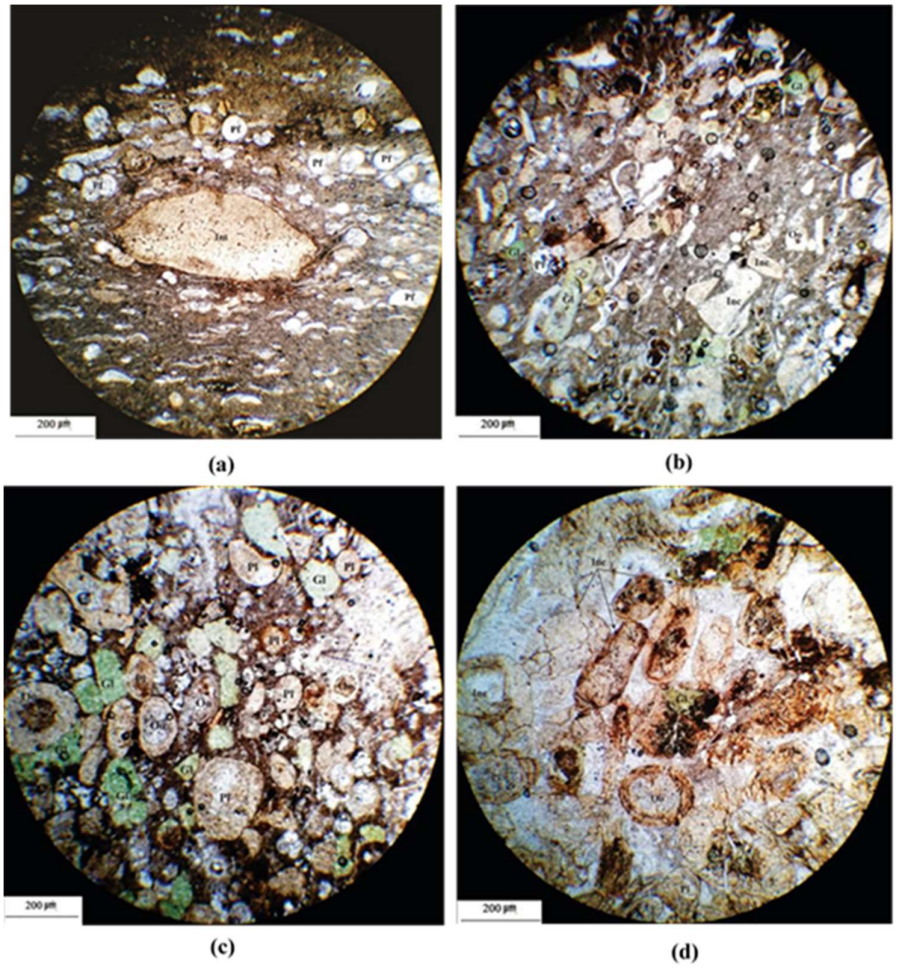

Figure16. (A) Packstone microfacies shell-lag beds. XPL; 200X. (b) Packstone with phosphatized foraminiferal tests that is bioclastic, intraclastic, and foraminiferal. XPL; 40X. (c) (c). Packstone that is bioclastic, glauconitic, intraclastic, and ooid and contains tiny phosphatized foraminiferal tests and fossilized fish scales and bones. XPL; 200X. (d) (d). Bioclastic, oolitic, phosphatic, foraminiferal grainstone that is well-balanced and well-sorted. There are also some phosphatized foraminifera and phosphatic intraclasts. XPL; 200X. Foraminiferal abbreviations include Bf (benthic), Pf (planktonic), Pl (pellet), Oo (ooid), Inc (intraclast), and Gl (glauconite).

Journal of New Zealand Studies NS35 (2023), https://doi.org/ 10.5281/zenodo.7805493

These microfacies are thought to have been deposited as carbonate tempestite, suggesting storm impacts on the ramp, and they are found in an outer ramp setting or close to the middle-outer ramp border [17]. Its microfacies is comparable to Wilson's standard microfacies (SMF 14) [22] and Ramp Carbonates' RMF 9 and RMF 29 [60]. This location received material from the inner ramp as a result of sporadic severe storm currents. Another distinguishing property of these microfacies is well-rounded, well-sorted bioclastic, phosphatic, foraminiferal oolitic grainstone (Figure 16d), which shows deposition in a shallow-water environment and is comparable to the RMF 29 of ramp carbonates [60].

The presence of packstone interbedded with bioturbated mudstones, frequently in upward fine grade form, ripple marks, and hummocky cross stratification (HCS), which are also found in field investigations, provide support for the storm's genesis in the phosphatic Pabdeh Formation (Figure 17a,b). These characteristics serve as reliable predictors of the storm wave base (SWB) at a height of 100 m [113].

(a) **(b)**

Figure 17. (a) Field sample of phosphatized horizon from the Siah section showing hummocky cross stratification. (b) Ripple marks on top of phosphatic layers in the phosphatized horizon from the Siah section.

- Bioclastic foraminiferal/algal packstone with large benthic foraminifera and crinoids

This microfacies, which has an overall thickness of roughly 164 m, is made up of the top portions of the Pabdeh Formation. Algae, benthic foraminifera like Ditropa sp. and Operculina sp. (Supplementary), crinoids, and bryozoans are all present in them (e.g. Tubucellaria sp.). Little amounts of fossils are present in the planktonic foraminifera (Figure 18a,b). Algae and benthic foraminifera make up the majority of this microfacies. When Paragloburotalia kugleri initially appears, the upper border of these microfacies may be identified [114]. From a lithological perspective, the transition from the medium-bedded packstone of the Pabdeh Formation, which contains thin marl and limestone particles, to the massive bedded, cliff-forming limestone of the Asmari Formation, which contains large benthic foraminifera, marks the contact with the overlying Asmari Formation [17]. The border between the Pabdeh and Asmari formations may be identified by the first occurrence of thick to massive bedded limestone.

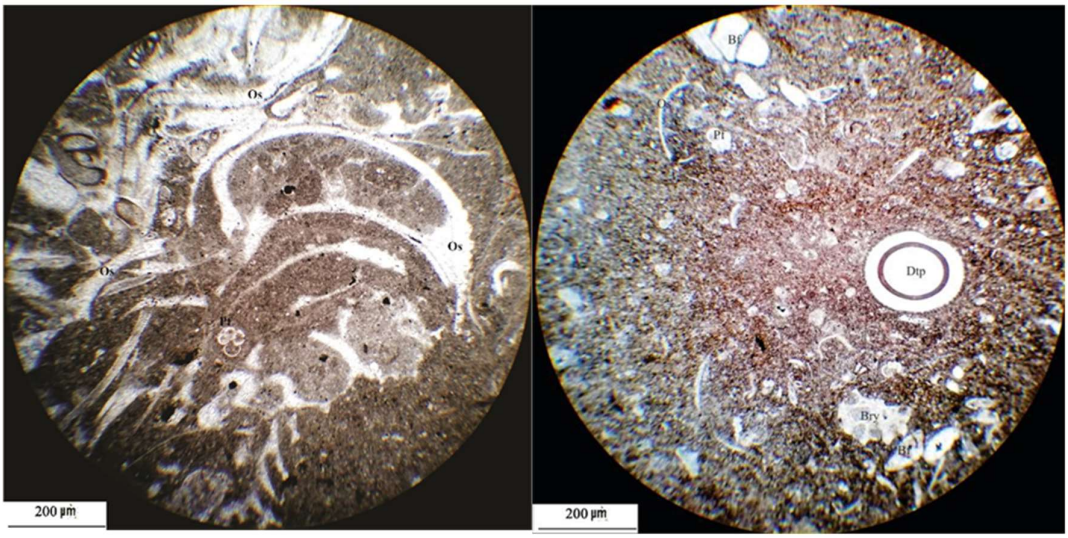

Figure 18. (a) Bioclastic foraminiferal algal packstone with large benthic foraminifera, ostracoda and bryozoan. (b) Bioclastic foraminiferal packstone with benthic foraminifera, bryozoan and ditropa. Dtp: Ditropa; Bry: Bryozoa; Bf: Benthic foraminifera; Pf: Planktonic foraminifera; Os: Ostracoda.

5. Discussion

Echinoderms, planktonic and benthic foraminifera, bryozoans, and radiolaria are examples of the faunal association of the Pabdeh Formation. In contrast to the tropical chlorozoan association, these communities are found in temperate and cold water as well as in deeper environments [60,115].

Ripple marks, hummocky cross stratification (HCS), grainstone microfacies, the presence of bioclastic carbonates containing shallow water faunas in hemipelagic environments, burrow structures, shell lags, and the alternation of packstone and mudstone laminae, which are also identified in field studies, are examples of sedimentological structures that indicate episodes of intense storm-generated currents activities. In the deeper portions of the basin, these storm currents brought carbonate sediments, which were then deposited on top of mudstone with an erosional contact [17]. The Pabdeh Formation was formed on a carbonate ramp setting that was influenced by repeated storm conditions, according to the conclusions of the depositional conditions of the facies. Although there is no evidence of evaporative precipitation or a restricted hypersaline microfauna in the upper portions of the Pabdeh Formation, the presence of algae and the abundance of benthic foraminifera (family Nummulitidae) suggest that this microfacies was deposited in or near the middle-outer ramp boundary and are interpreted to have been deposited as carbonate tempestite, indicating storm influences on the ramp [17].

While oceanic circulation, upwelling processes, and cold nutrient-rich currents rising to the ocean surface were not engaged in the creation of the phosphate horizons, storm events had a substantial impact on the phosphate deposition in the deep portions of the Pabdeh Formation.

The absence of facies consistent with a rimmed shelf habitat, such as a shallow protected rimmed shelf with a shoal, points to a distally steepened ramp as the Pabdeh Formation's depositional environment. From the back-shoal setting to the center of the ramp, storm currents in shallow

sections produced well-rounded, well-sorted foraminiferal oolitic grainstone. The lack of either a slope break or abrupt facies shifts from the platform to the deep basin [17] is another support for the Pabdeh Formation's ramp setting. The Pabdeh Formation was most likely formed on a carbonate ramp setting in this region, as shown by the lack of any marginal reef growth, the presence of pelagic microfauna, and low-energy mudstone facies.

The standard microfacies (SMF 3) of Wilson [22] and RMF 5 of ramp carbonates [60] are comparable to the bioclastic mudstone/wackestone microfacies of the Pabdeh Formation. The standard microfacies (SMF 8) of Wilson [22] and RMF 3 of ramp carbonates [60] are comparable to the buried bioclastic wacke/packstone with a variety of fossils from this formation.

The central and outside portions of the ramp held the majority of the sediments that made up the Pabdeh Formation. Storm currents and turbidity systems drove the dispersion of these sediments in this area.

The mudstone and wacke to packstone laminations are altered in the middle and outer ramp sediments, which are composed of repeating facies. Sediments were brought to these areas of the ramp by sporadic storm currents, creating a cyclic pattern of facies in the center and outer ramp setting. Under the impact of marine currents, stratigraphically open marine outer-ramp pelagic facies eventually transformed into middle-ramp facies. A shallow carbonate ledge (the Asmari Formation) was deposited over the Pabdeh Formation as an overlaying blanket during the last stage of ramp formation [116,117]. The main characteristics of the Pabdeh Formation are well accepted, however there is ongoing discussion on the palaeobathymetry of the pelagic deposits.

The Pabdeh Formation's well-rounded, well-sorted bioclastic, oolitic, and phosphatic grainstone indicates shallow-water deposits from a facies that was previously believed to be deep pelagic. In these pelagic environments, sinking-upward cycles—some of which have prograding oolitic shoals at the top—reappear. Phosphatic grains and intraclasts from shallow habitats were successively winnowed, transported, and redeposed by storm-generated currents to produce phosphatic grainstone. The largest concentrations of Mo, Zn, and Sb were found in the Mondun section, according to the trace element pattern, whereas the highest concentrations of Ba, As, Cd, Cr, Cu, Ni, Sc, Sr, Th, V, and Zr were found in the phosphatic particles from the Nill section. It has been suggested that the Nill phosphatic layers' enriched concentrations of Cu, Ni, and Zn are indicative of organic material produced from marine plankton [118,119]. The best indicators of organic carbon flux, which serves as a gauge of surface-water productivity, are copper and nickel [120]; the highest enrichment of Ba, As, Cd, Cr, Cu, Ni, Sc, Sr, Th, V, and Zr in the Nill and Siah sections is probably due to the presence of low-grade P2O5.

The tiny amounts of glauconite, ferromagnesian, and pyrite minerals in the sediments can be attributed to the Mondun phosphorites' low iron concentrations. For each part, the Fe2O3 content is close to 2%. The Mondun portion has the greatest P2O5 concentration, although it also has significant levels of Mo, Zn, and Sb.

The phosphate layers of the Pabdeh Formation were created in middle and outer ramp setting circumstances, in contrast to the eastern Mediterranean and north and northwest Africa, where phosphate deposits occurred in shallow marine depositional habitats and evaporitic cycles.

In marine authigenic minerals, there is evidence for depth control on the size of Ce anomalies [94, 121, 122], where shallowing is linked to Ce depletion. Hence, the Nill section with Ce enrichment is thought to represent deeper water sedimentation, and the Mondun section with a decreased negative cerium anomaly (0.56) reflects highly reworked, bioturbated, and higher

energy realm. The depositional circumstances of the deep sea environment for this proposed Formation are further supported by REE data from the phosphatic layers of the Pabdeh Formation. Negative Ce anomalies define the Shale adjusted REE patterns of Mondun phosphorites. This anomaly suggests that the phosphate deposition took place in an oxic environment.

These geochemical results are consistent with microfacies analyses, which show that the Mondun section is in a shallow and high energy state with negative cerium anomalies, whereas the Nill and Siah sections are in a deep ramp setting with positive cerium anomalies in REE patterns.

6. Conclusion

The Nill, Mondun, and Siah basins in south-western Iran are ramp settings where significant Eocene-Oligocene phosphate-bearing deposits are found.

The following are the main findings from the analysis of these three sites.

At the three outcrop sections under study, four lithofacies were found: I bioclastic foraminiferal/algal/peloidal packstone; (ii) burrowed bioclastic wacke/packstone with a variety of fossils; (iii) graded, laminated, and phosphatized-bedded bioclastic packstone.

In the Nill, Mondun, and Siah anticlines, the majority of the carbonate strata from the Pabdeh Formation were deposited in Moderate to outer ramp settings.

The first phosphatic horizon in all the sections is of middle Eocene age (Lutetian stage), according to biostratigraphic analyses of planktonic foraminifera and the presence of Orbulinoides beckmani (Supplementary); the second and third horizons are Bartonian.

Globally speaking, the Pabdeh Formation may be regarded as a low-grade mineral deposit. The typical phosphorite content of Tethyan phosphate deposits is 25–30%, whereas the average phosphate content of the Pabdeh Formation is 8–12% P2O5.

Microfacies studies show that turbidity currents helped all the phosphatic ooids and phosphatized foraminifera, fish scales, bones, and phosphatic intraclasts move from shallow regions of the Tethyan Ocean to deeper regions. These regions include the eastern Mediterranean, north and northwest Africa, such as Tunisia, Iraq, Saudi Arabia, Morocco, and Algeria. Phosphate particles were carried by storm-generated waves to the ocean's deeper inner ramp, where they were suspended and alternatively deposited as shell-lag and phosphate laminations. This is the first account of the deposition of phosphate-bearing horizons, which were previously believed to develop in nutrient-rich currents. The three portions of the Pabdeh Formation have unique geochemical fingerprints, as shown by major-element, TE, and REE+Y data from the phosphorites.

Strong positive inter-elemental correlations exist between all of the REE+Y and P2O5, attesting to the group's great geochemical coherence. The Nill portion with Ce enrichment is thought to indicate deeper water sedimentation, whereas the Mondun part with a decreased negative cerium anomaly (0.56) suggests highly reworked, bioturbated, and higher energy realm.

Conflict of interest

The authors declare no conflict of interest in publishing this article.

References

1. Versfelt Jr PL (2001) Major Hydrocarbon potential in Iran. In: Downey MW, Threet JC, Morgan WA, Petroleum provinces of the twenty first century. American Association of

Petroleum Geologists Memorial 74: 417–427.
2. Alavi M (2004) Regional stratigraphy of the Zagros fold-thrust belt of Iran and its proforeland evolution. Am J Sci 304: 1–20.
3. James GA, Wynd JG (1965) Stratigraphic Nomenclature of Iranian Oil Consortium Agreement Area. AAPG Bull 49: 2182–2245.
4. Ala MA, Kinghorn RRF, Rahman M (1980) Organic geochemistry and source rock characteristics of the Zagros petroleum province: South West Iran. J Pet Geol 3: 6l–89.
5. Bordenave ML, Bunwood R (1990) Source rock distribution and maturation in the Zagros orogenic belt-provenance of the Asmari and Bangestan reservoir oil accumulations. Org Geochem 16: 369–378.
6. Bordenave ML, Huc AY (1995) The Cretaceous source rocks in the Zagros Foothills of Iran. Rev Inst Fr Pet 50: 721–752.
7. Daraei M, Amini A, Ansari M (2015) Facies analysis and depositional environment study of the mixed carbonate–evaporite Asmari Formation (Oligo-Miocene) in the sequence stratigraphic framework, NW Zagros, Iran. Carbonates Evaporites 30: 253–272.
8. Berberian M, King GCP (1981) Towards a paleogeography and tectonic evolution of Iran. Can J Earth Sci 18: 210–265.
9. Lees GM, Falcon NL (1952) The geographical history of the Mesopotamian plains. Geogr J 118: 24–39.
10. Purser BH (1973) Sedimentation around bathymetric highs in the southern Persian Gulf. In: Purser BH, The Persian Gulf: Holocene carbonate sedimentation and diagenesis in a shallow epicontinental sea, Berlin and New York: Springer-Verlag, 157–177.
11. Kassler P (1973) The structural and geomorphic evolution of the Persian Gulf. In: PurserBH, The Persian Gulf: Holocene carbonate sedimentation and diagenesis in a shallow epicontinental sea, Berlin and New York: Springer-Verlag, 11–32.
12. Baltzer F, Purser BH (1990) Modern alluvial fan and deltaic sedimentation in a foreland Tectonic setting: the lower Mesopotamian plain and the Arabian Gulf. Sediment Geol 67: 175–195.
13. Stocklin JA (1974) Northern Iran: Alborz Mountains, Mesozoic–Cenozoic orogenic Belt, data for orogenic studies. Geological Society of London Special Publication 4: 213–234.
14. Takin M (1972) Iranian geology and continental drift in the Middle East. Nature 235: 147–150.
15. Alavi M (2007) Structures of the Zagros fold-thrust belt in Iran. Am J Sci 307: 1064–1095.
16. Sharland PR, Archer DM, Casey RB, et al. (2001) Arabian plate sequence stratigraphy. Gulf Petro link: Manama, Bahrain, 371–384.
17. Mohseni H, Al-Aasm IS (2004) Tempestite deposits on the storm influenced carbonate ramp: An example from the Pabdeh Formation (Paleogene), Zagros basin, SW Iran. J Pet Geol 27: 163–178.
18. Mohseni H, Behbahani R, Khodabakhsh S, et al. (2011) Depositional environments and trace fossil assemblages in the Pabdeh Formation (Paleogene). Zagros Basin, Iran. Neues Jahrb Geol Paläontol 262: 59–77.
19. Bolourchifard F, Fayazi F, Mehrabi B, et al. (2019) Evidence of high-energy storm and shallow water facies in Pabdeh sedimentary phosphate deposit, Kuhe-Lar-anticline, SW Iran.

Carbonate Evaporite 34: 1703–1721.
20. Bahrami M (2009) Microfacies and Sedimentary Environments of Gurpi and Pabdeh Formations in Southwest of Iran. Am J Appl Sci 6: 1295–1300.
21. Rezaee P, Nejad SAA (2014) Depositional evolution and sediment facies pattern of the tertiary basin in southern Zagros, South Iran. Asian J Earth Sci 7: 27–39.
22. Wilson JL (1975) Carbonate Facies in Geologic History. Berlin, Germany: Springer-Verlag, 471.
23. Carozzi AV, Gerber MS (1978) Sedimentary Chert Breccia: A Mississippian Tempestite. J Sediment Pet 48: 705–708.
24. Bourgeois JA (1980) Transgressive Shelf Sequence Exhibiting Hummocky Stratification: The Cape Sebastian Sandstone (Upper Cretaceous), Southwestern Oregon. J Sediment Pet 50: 681–702.
25. Kreisa RD (1981) Storm-Generated Sedimentary Structures in Subtidal Marine with Examples from the Middle and Upper Ordovician of Southwestern Virginia. J Sediment Pet 51: 823–848.
26. Walker RG (1984) General Introduction: facies, facies sequences and facies models. In: Walker RG, Facies Models, Canada: Geoscience, 1–9.
27. Vera JA, Molina JM (1998) Shallowing-upward cycles in pelagic troughs. (Upper Jurassic, Subbetic, Southern Spain). Sediment Geol 119: 103–121.
28. Cheel RJ, Leckie DA (1993) Coarse grained storm beds of the upper Cretaceous Chungo Member (Wapiabi Formation), Southern Alberta, Canadian. J Sediment Pet 62: 933–945.
29. Molina JM, Ruiz-Ortiz PA, Vera JA (1997) Calcareous tempestites in pelagic facies (Jurassic, Betic Cordilleras, Southern Spain). J Sediment Pet 109: 95–109.
30. Hips K (1998) Lower Triassic storm-dominated ramp sequence in northern Hungary: an example of evolution from homoclinal through distally steepened ramp to Middle Triassic flat-toped platform. In: Wright V., Burchette TP, Carbonate Ramps, London: Geological Society of London, Special Publication, 149: 315–338.
31. Abed AM (2013) The eastern Mediterranean phosphorite giants: An interplay between tectonics and upwelling. GeoArabia 18: 67–94.
32. Jasinski SM (2003) Phosphate rock. United States Geological Survey Minerals Yearbook, 56.1–56.5.
33. Jasinski SM (2011) Phosphate rock. Mineral Commodity Summaries 2011, United States Geological Survey, United States Government Printing Office, Washington, D.C.
34. Van Kauwenbergh SJ (2010) World phosphate rock reserves and resources. International Fertilizer Development Center (IFDC), Technical Bulletin no. 75, Muscle Shoals, Alabama, USA, 58.
35. Lucas J, Prévôt L (1975) Les marges continentales, pièges géochimiques, l'example de la marge atlantique de l'Afrique a la limite Crétacé-Tertiaire. Bull Soc Géol Fr 7: 496–501.
36. Notholt AJG (1980) Economic phosphatic sediments-mode of occurrence and stratigraphical distribution. J Geol Soc Lond 137: 793–805.
37. Lucas J, Prévôt L (1995) Tethyan phosphates and bioproductites. In: Nairn AEM, Stehli FG, The Ocean Basins and Margins—The Tethys Ocean. Plenum Press, 8, 367–391.
38. Follmi KB (1996) The phosphorus cycle, phosphogenesis and marine phosphate-rich deposits. Earth-Sci Rev 40: 55–124.

39. Soudry D, Glenn CR, Nathan Y, et al. (2006) Evolution of the Tethyan phosphogenesis along the northern edges of the Arabian-African shield during the Cretaceous–Eocene as deduced from temporal variations in Ca and Nd isotopes and rates of P accumulation. Earth-Sci Rev 78: 27–57.
40. Al-Bassam KS (1989) The Akashat phosphate deposits, Iraq, In: NothoIt AJG, Sheldon RP, Davison DF, Phosphate Deposit of the World, Phosphate Rock Resources, Cambridge Univ. Press, 2: 316–322.
41. Jones RW, Racey A (1994) Cenozoic stratigraphy of the Arabian Peninsula and Gulf. In: Simmons MD, Micropalaeontology and Hydrocarbon Exploration in the Middle East. London, Chapman and Hall, 273-307.
42. Bramkamp RA (1941) Unpublished report: In: Cavelier C, Geological description of the Qatar Peninsula. Qatar, Bureau de recherches géologiques et minières, 39.
43. Soudry D, Nathan Y, Ehrlich S (2013) Geochemical diagenetic trends during phosphorite formation-economic implications: The case of the Negev Campanian phosphorites, Southern. Sedimentology 60: 800–819.
44. Follmi KB, Garrison RE (1991) Phosphatic sediments, ordinary or extraordinary deposits? The example of the Miocene Monterey Formation (California). In: Muller DW, McKenzie JA, Weissert H. Geologic Events and Non-Uniform Sedimentation, London, Academic Press, 55–84.
45. Zaïer A, Beji-Sassi A, Sassi S, et al. (1998) Basin evolution and deposition during the Early Paleocene in Tunisia. In: Macgregor DS, Moody RTJ, ClarkLowes DD, Petroleum Geology of North Africa. London, Geological Society of London Special Publication, 132: 375–393.
46. Burollet PF (1956) Contribution à l'étude stratigraphique de la Tunisie Centrale. Ann Mines Géol 18: 352.
47. Fournier D (1978) Nomenclature lithostratigraphique des série du Crétacé supérieur au Tertiaire de Tunisie. Bull Cent Rech Explor Prod Elf-Aquitaine 2: 97–148.
48. Sassi S (1974) La sédimentation phosphatée au Paléocène dans le Sud et le Centre Ouest de la Tunisie. Unpublished thesis Doctorat. d'Etat ès-Sciences, Université de Paris-Orsay, France, 300.
49. Chaabani F (1995) Dynamique de la partie orientale du bassin de Gafsa au Crétacé ET au Paléogène: Etude minéralogique ET géochimique de la série phosphate Eocène, Tunisie méridionale. Thèse Doc. Etat, Univ. Tunis II. Tunisie.
50. Henchiri M, Slim-S'Himi N (2006) Silicification of sulfate evaporites and their carbonate replacement in Eocene marine sediments, Tunisia, two diagenetic trends. Sedimentology 53: 1135–1159.
51. Chaabani F, Ounis A (2008) Sequence stratigraphy and depositional environment of phosphorite deposits evolution: case of the Gafsa basin, Tunisia. Conference abstract at the Intern. Geol. Cong. Oslo.
52. Galfati I, Sassi AB, Zaier A, et al. (2010) Geochemistry and mineralogy of Paleocene–Eocene Oum El Khecheb phosphorites (Gafsa-Metlaoui Basin) Tunisia. Geochem J 44: 189–210.
53. Kocsis L, Gheerbrant E, Mouflih M, et al. (2014) Comprehensive stable isotope investigation of marine biogenic apatite from the late Cretaceous-early Eocene phosphate series of Morocco. Palaeogeogr Palaeoclimatol Palaeoecol 394: 74-88.
54. Messadi AM, Mardassi B, Ouali JA, et al. (2016) Sedimentology, diagenesis, clay

mineralogy and sequential analysis model of Upper Paleocene evaporitecarbonate ramp succession from Tamerza area (Gafsa Basin: Southern Tunisia). J Afr Earth Sci 118: 205-230.
55. El-Naggar ZR, Saif SI, Abdennabi A (1982) Stratigraphical analysis of the phosphate deposits in Northwestern Saudi Arabia. Progress report 1-4 submitted to SANCST, Riyadh. Saudi Arabia.
56. Baioumy H, Tada R (2005) Origin of Late Cretaceous phosphorites in Egypt. Cretaceous Res 26: 261–275.
57. Scotese CR (2014) The PALEOMAP Project Paleo Atlas for ArcGIS, version 2, Volume 1, Cenozoic Plate Tectonic, Paleogeographic, and Paleoclimatic Reconstructions, PALEOMAP Project, Evanston, IL, Maps 1–15.
58. Wade BS, Pearson PN, Berggren, WA, et al. (2011) Review and revision of Cenozoic tropical planktonic foraminiferal biostratigraphy and calibration to the geomagnetic polarity and astronomical time scale. Earth-Sci Rev 104: 111–142.
59. Dunham RJ (1962) Classifications of carbonate rocks according to depositional texture. In: Ham WE, Classification of Carbonate Rocks--A Symposium, AAPG Special Publications, 108–121.
60. Flugel E (2010) Microfacies of Carbonate Rocks, Analysis, Interpretation and Application. 2nd Edition. Berlin: Springer-Verlag, 984.
61. Omidvar M, Safari A, Vaziri-Moghaddam H, et al. (2016) Facies analysis and paleoenvironmental reconstruction of upper cretaceous sequences in the eastern Para-Tethys basin, NW Iran. Geol Acta 14: 363–384.
62. Baioumy H, Omran M, Fabritius T (2017) Mineralogy, geochemistry and the origin of high-phosphorus oolitic iron ores of Aswan, Egypt. Ore Geol Rev 80: 185–199.
63. Donnelly TH, Shergold JH, Southgate PN, et al. (1990) Events leading to global phosphogenesis around the Proterozoic-Cambrian transition. In: Notholt AJG, Jarvis I, Phosphorite research and development. London: Journal Geology Society London. Special Publication, 52: 273–287.
64. Trappe J (1998) Phanerozoic phosphorite depositional systems: A dynamic model for a sedimentary resource system. Lecture Notes in Earth Science 76: 1–316.
65. Piper DZ (1991) Geochemistry of a Tertiary sedimentary phosphate deposit: Baja California Sur, Mexico. Chem Geol 92: 283–316.
66. Soudry D, Ehrlich S, Yoffe O, et al. (2002) Uranium oxidation state and related variations in geochemistry of phosphorites from the Negev (southern). Chem Geol 189: 213–230.
67. Jarvis I, Burnett WC, Nathan Y, et al. (1994) Phosphorite geochemistry: state-of-the-art and environmental concerns. Eclogae Geol Helv 87: 643–700.
68. Garnit H, Bouhlel S, Jarvis I (2017) Geochemistry and depositional environments of Paleocene-Eocene phosphorites: Metlaoui Group, Tunisia. J Afr Earth Sci 134: 704–736.
69. McArthur JM (1985) Francolite geochemistry-compositional controls during formation, diagenesis, metamorphism and weathering. Geochim Cosmochim Acta 49: 23–35.
70. McArthur JM (1978) Systematic variations in the contents of Na, Sr, CO2 and SO4 in marine carbonate fluorapatite and their relation to weathering. Chem Geol 21: 41–52.
71. Altschuler ZS (1980) The geochemistry of trace elements in marine phosphorites. Part I: characteristic abundances and enrichment. In: Bentor YK, Marine Phosphorites. London: SEPM Special Publication, 29: 19–30.

72. Prévôt L (1990) Geochemistry, Petrography, Genesis of Cretaceous-Eocene Phosphorites. Soc Geol Fr Mem 158: 1–232.
73. Jiang SY, Zhao HX, Chen YQ, et al. (2007) Trace and rare earth element geochemistry of phosphate nodules from the lower Cambrian black shale sequence in the Mufu Mountain of Nanjing, Jiangsu province, China. Chem Geol 244: 584–604.
74. Prevot L, Lucas J (1980) Behaviour of some trace elements in phosphatic sedimentary formations. Society of Economic Paleontologists and Mineralogists, Special Publication 29: 31–40.
75. Gulbrandsen RA (1966) Chemical composition of the phosphorites of the Phosphoria Formation. Geochim cosmochim Acta. 30: 769–778.
76. Slansky M (1986) Geology of sedimentary phosphate (Studies in Geology). 1st English edition. North Oxford Academic Publishers Limited, 59–159.
77. Iylin AV, Volkov RI (1994) Uranium Geochemistry in Vendian-Cambrian Phosphorites. Geokhimiya 32: 1042–1051.
78. Sokolov AS (1996) Evolution of Uranium Mineralization in Phosphorites. Geokluntiva 11:1117–1119.
79. Zanin YN, Zanrirailova AG, Gilinskaya LG, et al. (2000) Uranium in the Sedimentary Apatite during Catagenesis. Geokhimiya 5: 502–509.
80. Baturin GN, Kochenov AV (2001) Uranium in phosphorites. Lithol Miner Resour 36: 303–321.
81. Smirnov KM, Men'shikov YA, Krylova OK, et al. (2015) Form of Uranium Found in Phosphate Ores in Northern Kazakhstan. At Energy 118: 337–340.
82. Cunha CSM, da Silva YJAB, Escobar MEO, et al. (2018) Spatial variability and geochemistry of rare earth elements in soils from the largest uranium-phosphate deposit of Brazil. Environ Geochem Health 40: 1629–1643.
83. Lucas J, Prevot J, Larnboy M (1978) Les phosphorites de in marge norde de I' Espagne, Cl imie mineralogy, Genese. Oceanol Acta 1: 55–72.
84. Saigal N, Banerjee DM (1987) Proterozoic phosphorites of India: updated information. Part 1: Petrography. In: Kale VS, Phansalkar VG, Purana Basins of Peninsular India. India: Geological Society of India Memoir, 6: 471–486.
85. Dooley JH (2001) Baseline Concentrations of Arsenic, Beryllium and Associated Elements in Glauconite and Glauconitic Soils in the New Jersey Coastal Plain. The New Jersey Geological Survey, Investigation Report, Trenton NJ, 238.
86. Barringer JL, Reilly PA, Eberl DD, et al. (2011) Arsenic in sediments, groundwater, and stream water of a glauconitic Coastal Plain terrain, New Jersey, USA. Appl Geochem 26: 763–776.
87. Liu YG, Mia MRU, Schmitt RA (1988) Cerium: A chemical tracer for paleo oceanic redox conditions. Geochim Cosmochim Acta 52: 2362–2371.
88. German CR, Elderfield H (1990) Application of the Ce anomaly as a paleoredox indicator: the ground rules. Paleoceanography 5: 823–833.
89. Murray RW, Brink MRB, Ten Gerlach DC, et al. (1991) Rare earth, major, and trace elements in chert from the Franciscan Complex and Monterey Group, California: Assessing REE sources to fine-grained marine sediments. Geochim Cosmochim Acta 55: 1875–1895.
90. Nath BN, Roelandts I, Sudhakar M, er al. (1992) Rare Earth Element patterns of the

Central Indian Basin sediments related to their lithology. Geophys Res Lett 19: 1197–1200.
91. Madhavaraju J, Ramasamy S (1999) Rare earth elements in Limestones of Kallankurichchi Formation of Ariyalur Group, Tiruchirapalli Cretaceous, Tamil Nadu. J Geol Soc India 54: 291–301.
92. Armstrong-Altrin JS, Verma SP, Madhavaraju J, et al. (2003) Geochemistry of Late Miocene Kudankulam Limestones, South India. Int Geol Rev 45: 16–26.
93. Madhavaraju J, González-León CM, Lee YI, et al. (2010) Geochemistry of the Mural Formation (Aptian-Albian) of the Bisbee Group, Northern Sonora, Mexico. Cretac Res 31: 400–414.
94. Wang YL, Liu YG, Schmitt RA (1986) Rare earth element geochemistry of South Atlantic deep sea sediments: Ce anomaly change at ~54 My. Geochim Cosmochim Acta 50: 1337–1355.
95. Kato Y, Nakao K, Isozaki Y (2002) Geochemistry of Late Permian to Early Triassic pelagic cherts from southwest Japan: implications for an oceanic redox change. Chem Geol 182: 15–34.
96. Kamber BS, Webb GE (2001) The geochemistry of late Archaean microbial carbonate: implications for ocean chemistry and continental erosion history. Geochim Cosmochim Acta 65: 2509–2525.
97. Kemp RA, Trueman CN (2003) Rare earth elements in Solnhofen biogenic apatite: geochemical clues to the palaeoenvironment. Sediment Geol 155: 109–127.
98. Bakkiaraj D, Nagendra R, Nagarajan R, et al. (2010) Geochemistry of Siliciclastic rocks of Sillakkudi Formation, Cauvery Basin, Southern India; Implications for Provenance. J Geol Soc India 76: 453–467.
99. McArthur JM, Walsh JN (1984) Rare-earth geochemistry of phosphorites. Chem Geol 47: 191–220.
100. Kidder DL, Krishnaswamy R, Mapes RH (2003) Elemental mobility in phosphatic shales during concretion growth and implications for provenance analysis. Chem Geol 198: 335–353.
101. Cossa M (1878) Sur la diffusion de cerium, du lanthane et du didyme, extract of a letter from Cossa to Sella, presented by Freny. C R Ac Sci 87: 378–388.
102. McKelvey VE (1967) Rare Earths in Western Phosphate Rocks. US Geological Survey Professional paper, 1–17.
103. Kocsis L, Gheerbrant E, Mouflih M, et al. (2016) Gradual changes in upwelled seawater conditions (redox, pH) from the late Cretaceous through early Paleogene at the northwest coast of Africa: negative Ce anomaly trend recorded in fossil bio-apatite. Chem Geol 421: 44–54.
104. Altschuler ZS, Berman S, Cuttiti F (1967) Rare earths in phosphorites-geochemistry and potential recovery. U. S. Geological Survey Professional paper, 575: 1–9.
105. Kon Y, Hoshino M, Sanematsu K, et al. (2014) Geochemical characteristics of apatite in heavy REE-rich deep-sea mud from Minami-Torishima area, southeastern Japan. Resour Geol 64: 47–57.
106. Taylor SR (1985) An examination of the geochemical record preserved in sedimentary rocks. In: Taylor SR, McLennan SM, The Continental Crust; Its composition and evolution, Blackwell, Oxford, 312.
107. Shields G, Stille P (2001) Diagenetic constraints on the use of cerium anomalies as palaeoseawater redox proxies: an isotopic and REE study of Cambrian phosphorites. Chem Geo 175: 29–48.

108. Elderfield H, Greaves MJ (1982) The rare earth elements in seawater. Nature 296: 214–219.
109. De Baar HJW, Bacon MP, Brewer PG (1985) Rare earth elements in the Pacific and Atlantic Oceans. Geochim Cosmochim Acta 49: 1943–1959.
110. Pattan JN, Pearce NJG, Mislankar PG (2005) Constraints in using Cerium-anomaly of bulk sediments as an indicator of paleo bottom water redox environment: A case study from the Central Indian Ocean Basin. Chem Geol 221: 260–278.
111. Daesslé LW, Carriquiry JD (2008) Rare Earth and Metal Geochemistry of Land and SubmarinePhosphorites in the Baja California Peninsula, Mexico, Mar Georesour Geotechnol 26: 340–349.
112. Stoneley R (1990) The Arabian continental margin in Iran during the late Cretaceous. In: Roberston AHF, Searl MP, Ries A, The geology and tectonics of the Oman region, London: Geological Society of London Special Publication, 49: 787–795.
113. Bolourchifard F, Fayazi F, Mehrabi B, et al. (2019) Evidence of high energy storm and shallow water facies in Pabdeh sedimentary phosphate deposit, Kuhe Lar anticline, SW Iran. Carbonate Evaporite 34: 1703–1721.
114. Daneshian J, Shariati Sh, Salsani A (2015) Biostratigraphy and planktonic foraminiferal abundance in the phosphate bearing pabdeh Formation of the lar mountains (SW Iran). Neues Jahrb Geol Paläontol 278: 175–189.
115. Rees A, Thomas A, Lewis M, et al. (2014) Lithostratigraphy and palaeoenvironments of the Cambrian in SW Wales. Geol Soc London 42: 33–100.
116. Vaziri-Moghaddam H, Kimiagari M, Taheri A (2006) Depositional environment and sequence stratigraphy of the Oligo-MioceneAsmari Formationin SW Iran. Facies 52: 41–51.
117. Murris RJ (1980) Middle East: stratigraphic evolution and oil habitat. Am Assoc Pet Geol Bull 64: 597–618.
118. Price NB, Calvert SE (1978) The geochemistry of phosphorites from the Namibian shelf. Chem Geol 23: 151–170.
119. Froelich PN, Arthur MA, Burnett WC, et al. (1988) Early diagenesis in organic matter in Peru continental margin sediments: Phosphorite precipitation. Mar Geol 80: 309–343.
120. Tribovillard N, Algeo TJ, Lyons T, et al. (2006) Trace metals as paleoredox and paleoproductivity proxies: an update. Chem Geol 232: 12–32.
121. MacLeod KG, Irving AJ (1996) Correlation of cerium anomalies with indicators of paleoenvironment. J Sediment Res 66: 948–988.
122. Shields G, Stille P, Brasier MD, et al. (1997) Stratified oceans and oxygenation of the late Proterozoic environment: a post glacial geochemical record from the Neoproterozoic of W Mongolia. Terra Nov 9: 218–222.